Cylindrical Photonic Crystals

by

Mihai Ibanescu

Submitted to the Department of Physics
in partial fulfillment of the requirements for the degree of

Doctor of Philosophy in Physics

at the

MASSACHUSETTS INSTITUTE OF TECHNOLOGY

June 2005

© Massachusetts Institute of Technology 2005. All rights reserved.

Author .....

Department of Physics
May 18, 2005

Certified by .....

John D. Joannopoulos
Francis Wright Davis Professor of Physics
Thesis Supervisor

Accepted by .....

Thomas J. Greytak
Associate Department Head for Education

MASSACHUSETTS INSTITUTE OF TECHNOLOGY
JUN 07 2005
LIBRARIES

ARCHIVES

Cylindrical Photonic Crystals

by

Mihai Ibanescu

Submitted to the Department of Physics
on May 18, 2005, in partial fulfillment of the
requirements for the degree of
Doctor of Philosophy in Physics

Abstract

In this thesis, we explore the properties of cylindrical photonic crystal waveguides in which light is confined laterally by the band gap of a cylindrically-layered photonic crystal. We show in particular that axially-uniform photonic band gap waveguides can exhibit novel behavior not encountered in their traditional index-guiding counterparts. Although the effects discussed in each chapter range from hollow-core transmission to zero and negative group velocity propagation and to high-Q cavity confinement, they are all a result of the photonic band gap guiding mechanism. The reflective cladding of the photonic crystal waveguide is unique in that it allows one to confine light in a low index of refraction region, and to work with guided modes whose dispersion relations lie above the light line of air, in a region where the longitudinal wave vector of the guided mode can approach zero.

Chapter 2 discusses hollow-core photonic band gap fibers that can transmit light with minimal losses by confining almost all of the electromagnetic energy to a hollow core and preventing it from entering the lossy dielectric cladding. These fibers have many similarities with hollow metallic waveguides, including the fact that they support a non-degenerate low-loss annular-shaped mode. We also account for the main differences between metal waveguides and photonic band gap fibers with a simple model based on a single parameter, the phase shift upon reflection from the photonic crystal cladding. In Chapter 3 we combine the best properties of all-dielectric and metallic waveguides to create an all-dielectric coaxial waveguide that supports a guided mode with properties similar to those of the transverse electromagnetic mode of a coaxial cable.

In Chapter 4, we introduce a mode-repulsion mechanism that can lead to anomalous dispersion relations, including extremely flattened dispersion relations, backward waves, and nonzero group velocity at zero longitudinal wave vector. The mechanism can be found in any axially-uniform reflective-cladding waveguide and originates in a mirror symmetry that exists only at zero longitudinal wave vector. In Chapter 5 we combine the anomalous dispersion relations discussed above with tunable waveguides to obtain new approaches for the time reversal (phase conjugation) and the time delay of light pulses.

Chapter 6 discusses a new mechanism for small-modal-volume high-Q cavities based on a zero group velocity waveguide mode. In a short piece of a uniform waveguide having a specially designed cross section, light is confined longitudinally by small group velocity propagation and transversely by a reflective cladding. The quality factor Q is greatly enhanced by the small group velocity for a set of cavity lengths that are determined by the dispersion relation of the initial waveguide mode.

In Chapter 7, we present a surprising result concerning the strength of band gap confinement in a two-dimensional photonic crystal. We show that a saddle-point van Hove singularity in a band adjacent to a photonic crystal band gap can lead to photonic crystal structures that defy the conventional wisdom according to which the strongest band-gap confinement is found at frequencies near the midgap.

Thesis Supervisor: John D. Joannopoulos
Title: Francis Wright Davis Professor of Physics

Acknowledgments

I am very grateful to Professor John D. Joannopoulos who was a wonderful advisor and a good friend during the past six years and a half. His excellent teaching skills brought me closer to his research group. His guidance, support, and enthusiasm made research work seem like play. I want to thank him for giving me the chance to get involved in so many interesting projects and for reminding me how exciting the work we were doing was when sometimes I felt otherwise. Last, but not least, I would like to thank him for the many group parties he organized at his house, and to congratulate him for the exquisite cranberry sauce he prepares each Thanksgiving.

My fellow group members along the years each deserve a thank you for making this a special group. Thank you Alex, Ardavan, Aristeidis, Casey, Chiyan, David Chan, David Roundy, Evan, Jiang, Lefteris, Maksim, Marin, Matt, Michelle, Michael, Niko, Peter Bermel, Peter Bienstman, Shanhui, Steven, and Tairan. And for those who graduated before me, thank you for showing me that great opportunities lie ahead. Professor Yoel Fink deserves special thanks for his constant enthusiasm about our research and for helping bring many of our theoretical ideas closer to reality.

I want to thank my family for their trust in me when I decided to continue my education abroad and for the support they gave me over the years. I would also like to thank my girlfriend Simona for being a wonderful person and for her support during the sometimes difficult process of writing this thesis.

Contents

1 Introduction **20**

1.1 Photonic Crystals and Photonic Band Gaps 20

1.2 Omnidirectional Reflectivity 21

1.3 Cylindrical Photonic Crystals 22

2 Hollow Cylindrical Photonic Band Gap Fibers **25**

2.1 Introduction 25

2.2 Hollow Waveguides 27

2.3 Calculation of Modes of the OmniGuide fiber 30

2.4 Comparison of OmniGuide Fiber Modes and Metal Waveguide Modes 32

2.5 Phase-Shift Model 37

2.6 Special Characteristics of the TE_{01} Mode 41

2.7 Recent Experimental Developments 46

2.8 Conclusions 47

3 An All-Dielectric Coaxial Waveguide **49**

3.1 Introduction 49

3.2 From Metallic to All-Dielectric Waveguides 52

3.3 Calculation of Coaxial Omniguide Modes 56

3.4 Modes of Coaxial Omniguide A 58

3.5 Single-Mode Behavior in Coaxial Omniguide B 60

3.6 Summary 64

4 Anomalous Dispersion Relations by Symmetry Breaking in Axially Uniform Waveguides 67

4.1 Introduction 67

4.2 Mode Symmetries in Axially Uniform Waveguides 68

4.3 Mode Repulsion Caused by Symmetry Breaking 70

4.4 Anomalous Dispersion Relations 72

4.5 Waveguide Designs 75

4.6 Summary 78

5 Phase Conjugation of Light Using a Negative Group Velocity Mode of an Axially-Uniform Waveguide 80

5.1 Introduction 80

5.2 Phase Conjugation 82

5.3 Time delay 82

5.4 Summary 82

6 Microcavity Confinement Based on Anomalous Zero Group-Velocity Waveguide Mode 85

6.1 Introduction 85

6.2 Zero Group Velocity at a Nonzero Longitudinal Wave Vector 86

6.3 New Mechanism for Confining Light 89

6.4 All-Dielectric High-Q Cavity 90

6.5 Summary 92

7 Enhanced Photonic Band-Gap Confinement via Van Hove Saddle Point Singularities 95

7.1 Introduction 95

7.2 Evanescent Modes of the Bulk Photonic Crystal 98
7.3 Enhanced Confinement via Saddle Point 99
7.4 General Arguments for the Existence of the Saddle Point 102
7.5 Summary 103

List of Figures

1-1 (a) Dielectric mirror made of alternating high and low index of refraction layers. The incoming light is at an angular frequency ω and has an angle of incidence θ. $k_{||}$ is the component of the wave vector parallel to the air/mirror interface. (b) Projected band structure of the dielectric mirror. Light blue areas represent $(\omega, k_{||})$ pairs for which propagating modes exist in the mirror. The yellow shaded area represents all frequency-wavevector combinations for which modes can propagate in air ($\omega > ck_{||}$) and is called the light cone. The two omnidirectional reflectivity ranges are shown in gray. 21

1-2 (a) A cylindrical waveguide is created by wrapping the omni-directional mirror from Fig. 1-1(a) into a circle. Light is reflected by the mirror for any angle of incidence from air and thus has to propagate along the fiber as shown in part (b), which is a schematic longitudinal cross-section of the waveguide. 22

1-3 (a) Part of preform after it was heated and drawn into fiber. (b) Hundreds of meters of thin, flexible fiber are obtained from a single preform. (c) Cross-section of a hollow-core photonic band gap fiber with a diameter of about 700 μm. The multilayered dielectric mirror can be seen as the thin lighter region immediately surrounding the core. (d) Magnified SEM of the hollow core, dielectric mirror, and polymer cladding. The inset shows the periodic arrangement of the chalcogenide and polymer layers. Images courtesy of Yoel Fink's group at MIT. . . 23

2-1 (Left) OmniGuide fiber of radius R. Light is confined in the hollow core by a multilayer dielectric mirror made of alternating layers with high (blue) and low (green) indices of refraction. (Right) Hollow metallic waveguide of radius R. Light is confined in the hollow core by a metallic cylinder. 28

2-2 (Left) Projected band structure associated with the dielectric mirror. The blue regions correspond to (k, ω) pairs for which light can propagate through the mirror. The meaning of the parallel wave vector k is shown in the inset. k_T is the transverse component of the wave vector. The diagonal black line represents the light line ($\omega = ck$). Shown in gray are two frequency ranges corresponding to omnidirectional reflectivity of the mirror. (Right) Frequency cutoffs of the lowest 11 modes supported by a hollow metallic waveguide are plotted versus the radius of the waveguide. TE polarized modes are shown in red, while TM modes are shown in blue. The number m in the labels is the angular momentum index of each mode. Note the degeneracy of the TE_{01} and the TM_{11} modes. The two thick vertical dashed lines correspond to radii $R = 2.0a$ and $R = 3.8a$, which are the values used for the two exemplary waveguides considered here. 29

2-3 Modes supported by an OmniGuide fiber of radius $R = 2.0a$ are shown with solid lines. Red is for TE and HE modes, while blue is for TM and EH modes. Only the first three modes are labeled in each band gap. The lowest three modes in a hollow metallic waveguide with the same radius are plotted as dots. 33

2-4 The lowest five modes supported by an OmniGuide fiber of radius $R = 3.8a$ are shown as solid red (TE or TE-like modes) and blue (TM or TM-like modes) curves. Higher modes exist, but are not shown. . . 34

2-5 The electric-field time-average energy density for the five modes in Fig. 4 is shown in a transverse cross section of the waveguide. The color scheme is such that the energy density goes from zero (black) to maximum (yellow). The thin blue contours represent the contours between the different layers of the OmniGuide fiber. For all five modes, the energy density is plotted for a frequency $\omega = 0.230\,(2\pi/a)$. 36

2-6 Combined phase shift and dispersion relation diagrams. Left panel: contour lines for the phase shift, $\Delta\phi$, are plotted together with the band gap of the dielectric mirror (white region), and the light line (black oblique line). The modes of the OmniGuide fiber with $R = 2.0a$ are shown as solid red/blue lines for TE/TM-like modes, while the modes in the metal waveguide are showed as dotted lines. The vertical arrows show the frequency difference between equivalent modes in the waveguides. The left and right panels are for modes with TE-like and TM-like polarization, respectively. The crossing between the OmniGuide HE_{11} mode and the metallic TE_{11} mode is shown as a black dot. 39

2-7 (Left) The confinement of electromagnetic energy in the hollow core of the OmniGuide fiber is plotted for three modes as a function of core radius. Actual data is shown as open circles. The solid lines represent fits as discussed in the text, and the dashed line is simply connecting the data points. (Right) The attenuation coefficient of the three modes is plotted as a function of radius. Also shown are the attenuation coefficient in silica fibers (0.2 dB/km) and a much larger attenuation coefficient (100 dB/km) assumed for the materials in the multilayer mirror. The circles and the lines have the same significance as in the left panel. 42

3-1 Schematics of coaxial waveguide cross sections: (a) traditional metallic coaxial cable; (b) coaxial omniguide, type A; and (c) coaxial omniguide, type B. In parts (b) and (c), the gray layers represent cylindric dielectric layers, with dark gray corresponding to the high dielectric constant material, and the light gray corresponding to the low dielectric constant material. For all cases (a–c), light can be confined within the coaxial region, shown in yellow, and guided along the axial z-direction. In (a) and (b) the inner and outer radii of the coaxial region are $r_i = 3.00a$ and $r_o = 4.67a$, whereas in (c) $r_i = 0.40a$ and $r_o = 1.40a$. 53

3-2 Projected band structures along an axial direction. (a) Traditional metallic coaxial cable with inner and outer coaxial radii of $r_i = 3.00a$ and $r_o = 4.67a$, respectively. The red bands correspond to allowed guided modes. For any given wavevector, the lowest frequency mode is a TEM mode characterized by a perfectly linear dispersion relation. The six next highest bands correspond to transverse electric (TE_{ml}) modes with $l = 1$ and increasing angular momentum m. (b) Omnidirectional, reflecting, all-dielectric multilayer film. Light-blue regions correspond to modes for which light is allowed to propagate within the dielectric mirror, and dark-blue regions correspond to modes for which light is forbidden to propagate within the dielectric mirror. The diagonal black line identifies the edge of the light cone. The horizontal gray lines mark the boundaries in frequency within which omnidirectional reflectivity is possible. (c) Coaxial omniguide A with inner and outer coaxial radii of $r_i = 3.00a$ and $r_o = 4.67a$, respectively, and bilayers consisting of indexes of refraction $n_1 = 4.6$ and $n_2 = 1.6$ and thickness $d_1 = 0.33a$ and $d_2 = 0.67a$, respectively. The red and yellow bands indicate guided modes confined to the coaxial region of the waveguide. The dashed lines indicate modes with less than 20% localization within the coaxial region. There is close correspondence between the modes labeled $m = 1$ to $m = 6$ and those of part (a) labeled TE_{11} to TE_{61}. Also, the yellow $m = 0$ mode corresponds to a TEM-like mode, as discussed in the text. 54

3-3 Power density in the electric field for guided modes at $k_z = 0.19\,(2\pi/a)$ in Fig. 3-2(c). Parts (a) through (d) correspond to guided modes with angular momenta $m = 0$ to $m = 3$, respectively. The color bar indicates that power increases in going from black to dark red, to red, to orange, to yellow. The blue circles identify the boundaries between the various dielectric shells and are included as a guide to the eye. Most of the power is confined to the coaxial region of the waveguide. The cylindrical symmetry and radial dependence of the $m = 0$ mode are consistent with those of a TEM mode. The small fluctuations in density away from perfect cylindrical symmetry in (A) are a consequence of the discrete square grid used in the computations. 59

3-4 Projected band structure for coaxial omniguide B. The central dielectric rod has an index of refraction $n_1 = 4.6$ and a radius $r_i = 0.40a$. The coaxial waveguiding region has an outer radius $r_o = 1.40a$, and the parameters of the outer bilayers are the same as those used for configuration A. The yellow dots represent confinement of the electric field power of more than 50%; the red dots represent confinement between 20 and 50%; and the dashed lines represent confinement less than 20%. The two white boxes identify the frequency ranges where the $m = 0$ band exhibits single-mode behavior. 62

3-5 Electric field for the mode at frequency $0.203\,(2\pi c/a)$ and $k_z = 0.2\,(2\pi/a)$ in Fig. 3-4. Parts (a) through (c) are the electric field components along the x, y, and z directions, respectively. The color bar indicates that large positive and negative values are shown as dark red and dark blue regions, respectively, whereas white areas represent regions of zero values of the electric field, and light-colored areas represent regions of low values of the electric field. The field distribution clearly reveals a high confinement of the mode in the coaxial waveguiding region, and in this region it is nearly completely transverse to the direction of propagation (less than 10^{-3} of the intensity is along z), as desired. 63

4-1 Top panel: Schematic drawings of the three types of reflective-cladding waveguides that employ metallic, multilayer-film, and photonic-crystal claddings. Bottom panel: Schematic band diagrams showing two neighboring modes as the relative frequency separation is decreased. At $k = 0$ one mode is TE polarized and the other TM polarized (the order is not important). (a) Weakly interacting modes. (b) A stronger interaction leads to a very flat lower band. (c) The repulsion between modes is strong enough to cause a backward wave region in the lower band. (d) Accidentally degenerate modes at $k = 0$ can have nonzero group velocity. 69

4-2 (a) Dispersion relations of two modes with angular momentum unity for the cylindrical waveguide in inset. The dark regions have an index of refraction 4.6 (*e.g.* Te), while the light gray regions have 1.4 (*e.g.* polymer). Starting from the center, the rod has a radius $0.45a$, the first ring has a thickness $0.32a$, the second one $0.23a$, and the following low/high index layers have thickness $0.75a/0.25a$, respectively. (b) Ultra-flattened dispersion relation in a photonic-crystal fiber with an index of refraction of 3.5 (*e.g.* semiconductor). The distance between two neighboring air holes is a and the radius of a normal hole is $0.46a$. The two dotted holes below the fiber core have a modified radius of $0.40a$. 76

5-1 Dispersion relations of the tunable waveguide for three values of the index of refraction of the central rod, $n_1 = 3.00$, 3.15, and 3.30. For wave vectors around 0.1 $(2\pi/R)$ the group velocity can be changed from positive to zero and even negative values. 81

5-2 The frequency spectrum of a pulse is flipped as a result of phase conjugation. 83

6-1 Band structure of the axially-uniform dielectric-loaded metal waveguide (inset) showing the lowest two modes. The lower mode is anomalous with a non-trivial point of zero group velocity at $k_0 = 0.146\,(2\pi/a)$, $\omega_0 = 0.1656\,(2\pi c/a)$. 87

6-2 (a) A piece of length L of the waveguide in Fig. 6-1 can form a high-Q cavity. (b) Resonant mode in cavity of length $L = 3.9a$. In an axial cross section, we show the electric field component perpendicular to the plane, with the red and blue regions corresponding to positive and negative values. The metal cladding is shown in black. Note that the FDTD computational cell is actually larger than the rectangular box shown here. (c) Resonant mode for $L = 13.9a$. (d) The quality factor Q is plotted as a function cavity length L. The red circles are the results of FDTD simulations, while the dashed vertical lines correspond to multiples of $\Lambda/2$. Also shown as a blue dashed line, is the $Q(L)$ curve for a cavity based on a modified waveguide that does not have $v_g = 0$ at $k \neq 0$. 88

6-3 (a) A cylindrical all-dielectric cavity. (b) The axial cross section shows the cavity structure: on top of a substrate with refraction index n_{sub}, we have a central rod with index n_1 followed by a region with index n_0 and surrounded by a Bragg mirror that confines light to the core region. The electric field component perpendicular to the plane is shown in a color plot. 91

7-1 (a) A waveguide is formed by removing one row from a 2D square lattice of dielectric rods with refractive index 3.4 and radius $r = 0.18a$. (b) The dispersion relation of the waveguide mode (thick black line) is shown on top of a color contour plot of the confinement strength of the bulk photonic crystal $\kappa(\omega, k_x)$. The black regions include (ω, k_x) pairs for which propagating modes exist in the bulk crystal, while the colors from dark red to bright yellow, represent increasingly stronger confinement, as shown by the colorbar. (c) Confinement strength κ along the dispersion relation of the guided mode. The gray areas delimit the complete band gap range. The y-axis is the same as in part (b). 97

7-2 The projected TM band structure of the bulk crystal is shown by the blue areas and the black lines that represent $\omega(k_x)$ curves at constant k_y values ranging from 0 to $0.5\,(2\pi/a)$ in steps of $0.05\,(2\pi/a)$. Note that the second band of bulk crystal has a saddle point singularity that is indicated by a thick black arrow. Also shown is the dispersion relation of the fundamental waveguide mode (red curve). 99

7-3 Dispersion relations $\omega(k_y^{(n)})$ at fixed k_x for propagating and evanescent modes in the bulk crystal. The axial wave vector k_x takes the values 0, 0.2, 0.3, and $0.5\,(2\pi/a)$ for parts (a) through (d). The imaginary part of $k_y^{(n)}$ is shown in red on the left side of each plot, while the real part is shown on the right, in blue for propagating modes and gray for evanescent and complex modes. In parts (a) and (c), the individual modes $k_y^{(n)}$ are labeled by the value of their n index. The A and B labels track the range of frequencies for which the $n = 0$ mode is evanescent, while the C label tracks the cutoff frequency of the $n = -1$ mode. . . 101

7-4 Contour plots of the second photonic crystal band $\omega(k_x, k_y)$ for varying radii of the dielectric rods: (a) $r = 0$ (vacuum), (b) $r = 0.06a$, (c) $r = 0.12a$, and (d) $r = 0.18a$. The same color scheme is used for all four parts of the figure. Constant-frequency contours are labelled by the corresponding value of the angular frequency ω in units of $(2\pi c/a)$. In parts (b), (c) and (d), a black dot indicates the position of the saddle point van Hove singularity. 102

List of Tables

2.1 Summary of comparison between OmniGuide fiber (OGF) modes and their hollow metallic waveguide (HMW) counterparts. The first three modes are taken from Fig. 3 for a radius $R = 2.0a$, and the next two are from Fig. 4, corresponding to $R = 3.8a$. 35

4.1 Possible Van Hove singularities in the density of states $D(\omega)$ corresponding to the lower mode in Fig. 4-1(a-d). 74

6.1 Conservation of round-trip phase shift. 90

Chapter 1

Introduction

1.1 Photonic Crystals and Photonic Band Gaps

Photonic crystals are periodic dielectric structures, with periodicity on the order of a wavelength, that alter the flow of light in ways not possible with traditional optical components [1, 2, 3, 4, 5]. The most dramatic behavior is found when the photonic crystal exhibits a complete band gap: a range of frequencies for which no propagating modes exist inside the crystal, and thus all incident light onto the crystal is reflected. This optical analogue to the electronic band gaps of semiconductors is very powerful as it allows for precise confinement and control of light inside photonic crystal devices such as cavities and waveguides. If spatial confinement in all three spatial directions is needed the perfect solution would be a photonic crystal with three-dimensional periodicity. Although continuous progress on such 3D crystals has been done in the past decade [6, 7], they are still rather difficult to fabricate. Self-assembly and holographic lithography techniques can lead to large volume bulk crystals, but don't allow for the easy introduction of useful defects. On the other hand, photo-lithography and e-beam lithography give control over the parameters of each unit cell, but become difficult to use if large volume 3D photonic crystals are required. In this thesis we

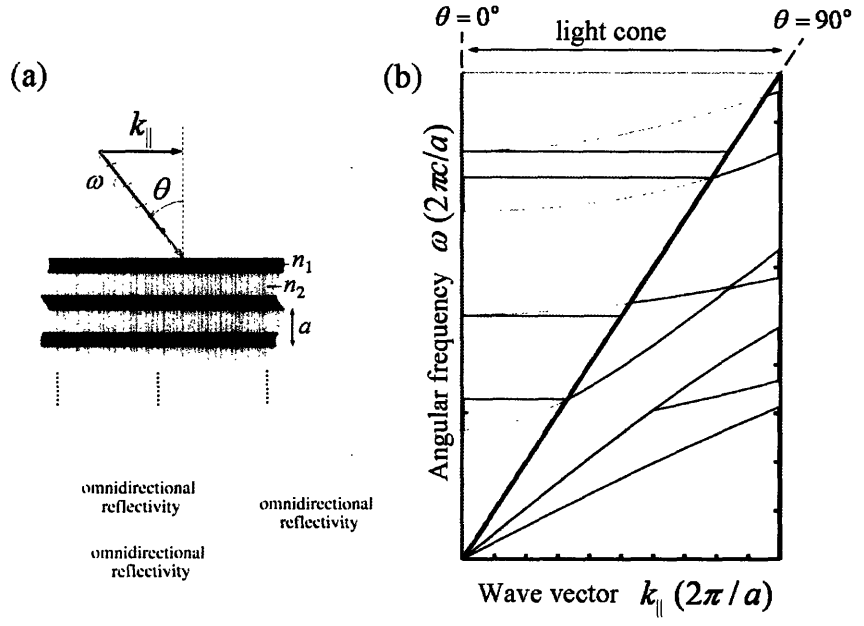

Figure 1-1: (a) Dielectric mirror made of alternating high and low index of refraction layers. The incoming light is at an angular frequency ω and has an angle of incidence θ. $k_{||}$ is the component of the wave vector parallel to the air/mirror interface. (b) Projected band structure of the dielectric mirror. Light blue areas represent $(\omega, k_{||})$ pairs for which propagating modes exist in the mirror. The yellow shaded area represents all frequency-wavevector combinations for which modes can propagate in air ($\omega > ck_{||}$) and is called the light cone. The two omnidirectional reflectivity ranges are shown in gray.

focus on photonic crystal structures that are periodic in only one direction. Even though these structures cannot provide a complete photonic band gap, they still can lead to many interesting physical effects and useful photonic devices, as illustrated by the chapters of this thesis.

1.2 Omnidirectional Reflectivity

Key to the optical properties of one-dimensionally periodic photonic crystals is the concept of omnidirectional reflectivity. Consider the semi-infinite multi-layered dielectric mirror of Fig. 1-1(a), made of alternating layers with high and low indices of refraction. Incoming from the air above is light with an angular frequency ω and

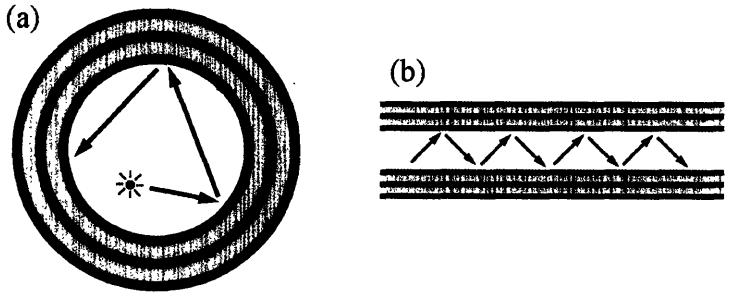

Figure 1-2: (a) A cylindrical waveguide is created by wrapping the omni-directional mirror from Fig. 1-1(a) into a circle. Light is reflected by the mirror for any angle of incidence from air and thus has to propagate along the fiber as shown in part (b), which is a schematic longitudinal cross-section of the waveguide.

an angle of incidence θ. If there exists a frequency range in which light is reflected from the mirror for any angle of incidence θ then we say that the mirror is an omnidirectional reflector. For a long time, it was believed that such one-dimensional omnidirectional reflectors are not possible because one-dimensionally periodic structures cannot have a complete photonic band gap. This can be understood with the help of Fig. 1-1(b) where we plot the $\omega(k_{||})$ band structure of the mirror, frequency versus parallel wave vector. As can be seen, there is no frequency range without any propagating modes in the mirror. However, when we consider light that is incident from air onto the mirror, the parallel wave vector $k_{||}$ is limited to be less than ω/c, which is shown in Fig. 1-1(b) as the yellow-shaded region. Overlapping this allowed light cone region on top of the dielectric mirror band structures, we find that there exist indeed two frequency ranges shown in gray, for which the incoming light cannot couple to any propagating modes of the mirror, no matter what the angle of incidence.

1.3 Cylindrical Photonic Crystals

Cylindrical photonic band gap waveguides can be realized by simply taking a strip of the omnidirectional dielectric mirror and rolling it around into a cylinder as shown in

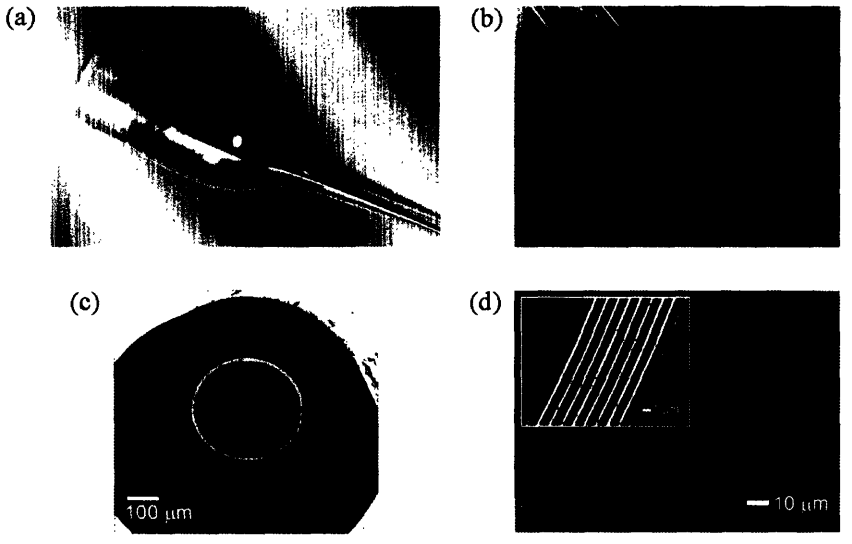

Figure 1-3: (a) Part of preform after it was heated and drawn into fiber. (b) Hundreds of meters of thin, flexible fiber are obtained from a single preform. (c) Cross-section of a hollow-core photonic band gap fiber with a diameter of about 700 μm. The multilayered dielectric mirror can be seen as the thin lighter region immediately surrounding the core. (d) Magnified SEM of the hollow core, dielectric mirror, and polymer cladding. The inset shows the periodic arrangement of the chalcogenide and polymer layers. Images courtesy of Yoel Fink's group at MIT.

Fig. 1-2. Light emitted inside of the waveguide or coupled into it cannot escape laterally because of the omnidirectional reflectivity properties of the cladding (coupling to cladding modes through evanescent tails is possible but limited to a narrow region near the cladding with a thickness comparable to a wavelength).

Before we move on to the various theoretical cylindrical photonic crystal designs of this thesis, it is important to mention that the first experimental steps towards actually implementing them in practice have already been taken. Fig. 1-3 describes the various steps involved in manufacturing a large-radius hollow-core photonic band gap fiber.

Chapter 2

Hollow Cylindrical Photonic Band Gap Fibers

Preface

This chapter is based in part on Ref. [8]: M. Ibanescu, S. G. Johnson, M. Soljacic, J. D. Joannopoulos, Y. Fink, O. Weisberg, T. D. Engeness, S. A. Jacobs, and M. Skorobogatiy, "Analysis of mode structure in hollow dielectric waveguide fibers," *Phys. Rev. E*, vol. 67, 046608 (2003). We also discuss recent experimental implementations of these fiber designs in Section 2.7.

2.1 Introduction

The advent of high-purity ultra-low-loss silica fiber as a transmission medium in the late 70's provided the basis for the modern optical communications infrastructure. Although highly successful, silica waveguides have fundamental limitations in their attenuation and non-linearities that result from the interaction of light with a dense, material-filled core. A different approach to waveguiding circumvents these problems by confining light in a hollow core using highly reflective walls. This approach is

exemplified by hollow metallic waveguides, which are very efficient in the millimeter wavelength range. Prior to the emergence of silica fiber, these waveguides were seriously considered as candidate media for long-distance telecommunications [9]. An impairment of metallic waveguides is that they become lossy at high frequencies due to the finite conductivity of metals. Thus, their use is restricted to low frequencies and this severely limits the ultimate bandwidth that they can transmit. By adding a dielectric coating on the inside of the metallic waveguide one can improve its properties. Such metallo-dielectric waveguides have been developed for infrared wavelengths, in particular for laser power delivery [10, 11].

Here we analyze an OmniGuide fiber – a hollow *all-dielectric* waveguide in which light is confined by an omnidirectional mirror [12]. The limitations that exist in both the silica fiber and the hollow metal waveguides can be systematically reduced in this waveguide due to its hollow core and the use of dielectric materials transparent at high frequencies.

Yeh *et al.* showed in 1978 that it is possible to transmit a non-index-guided mode in a multilayer cylindrical dielectric waveguide [13]. The radiative decay of the mode is suppressed using a Bragg reflector, *i.e.* a multilayered structure that is periodic in the radial direction. Initial work in this area has focused on structures based on doped-silica technology that have a low index contrast between the layers [14, 15, 16, 17]. These structures are useful, for example, to control the dispersion parameter of a fiber in ways that are not achievable in a standard silica fiber [17]. However, such structures cannot confine light primarily in a hollow core because of the large penetration of the field into the low index-contrast multilayer structure. Recently, with the discovery of the omnidirectional high-reflectivity properties of multilayer films [18, 19, 20], researchers have focused instead on high index contrast dielectric waveguides [21, 22, 23, 24, 25, 12, 26]. Fink *et al.* fabricated a large-core high index-contrast hollow dielectric waveguide and demonstrated that light is transmitted even

when tight bends are introduced in the waveguide, a result of the omnidirectionality of the dielectric mirror [21]. Xu *et al.* developed an efficient analytical method for calculating approximate dispersion relations of the modes of such waveguides, making use of the radial periodicity of the cladding layers [22]. Using this method, they calculated the number of layers required to suppress radiation as a function of the index contrast and substantiated that a large index contrast is necessary in order to limit the number of layers to a reasonable value [23]. Ibanescu *et al.* exploited the similarities between a dielectric multilayer mirror and a metal mirror and showed that it is possible to design an all-dielectric coaxial waveguide that supports a TEM-like mode [25].

In this chapter, we study the properties of a hollow dielectric waveguide in which light is confined by a large index-contrast omnidirectional dielectric mirror. The large index contrast produces a high degree of optical confinement in the core and results in a waveguide mode structure that is very similar to the mode structure of a hollow metallic waveguide. We present the similarities and differences between the hollow dielectric and metallic waveguides, and explain these results using a single-parameter model based on the phase shift upon reflection from the dielectric mirror. In addition, we show that the similarities between these two types of waveguides extend to their transmission properties in that they have the same lowest-loss mode, the TE_{01} mode.

2.2 Hollow Waveguides

The waveguides that we compare are shown in Fig. 2-1. On the left is depicted an OmniGuide fiber. A hollow core (index of refraction $n_0 = 1$) is surrounded by an omnidirectional mirror that consists of alternating layers having high and low indices of refraction [18]. The high/low index of refraction layers are shown in blue/green. The indices of refraction are 4.6/1.6 with corresponding thickness $0.33a/0.67a$, where a is

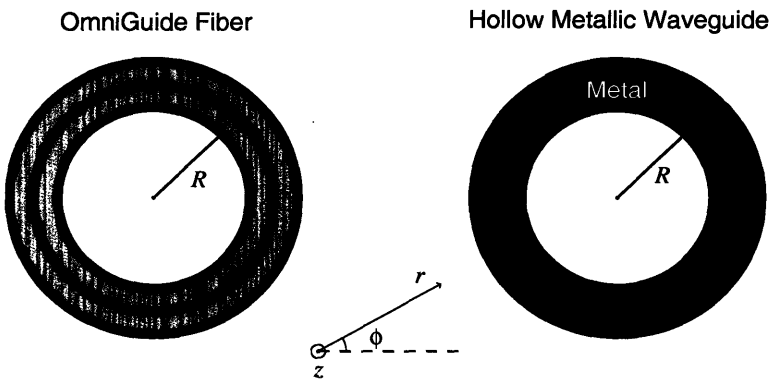

Figure 2-1: (Left) OmniGuide fiber of radius R. Light is confined in the hollow core by a multilayer dielectric mirror made of alternating layers with high (blue) and low (green) indices of refraction. (Right) Hollow metallic waveguide of radius R. Light is confined in the hollow core by a metallic cylinder.

the total thickness of a pair of layers. These values for the indices of refraction have been used in previous work [18, 21, 22, 23, 25, 12], including a fabricated multilayered waveguide operating at $10.6\,\mu m$. The large index contrast between the two types of layers allows us to better illustrate the comparison between the hollow dielectric and metallic waveguides; the conclusions are still valid for a smaller index contrast that one may have to use in practice. In the frequency range of omnidirectionality of the dielectric mirror the similarities between the two types of waveguides are enhanced because, in both cases, the mirror that confines light in the core is a very good reflector *for all angles of incidence and polarizations.* Moreover, the omnidirectionality of the dielectric mirror is important for practical considerations: in an imperfect waveguide, the coupling between the operating core mode and cladding modes above the light line is eliminated if the frequency of operation lies in the omnidirectional frequency range of the mirror.

The exact value of a in microns is determined by the wavelength of operation of the waveguide. For example, if one wants to use $\lambda = 1.55\mu m$, then the thickness of a bilayer should be chosen somewhere in the range $a = 0.3$–$0.4\mu m$. The radius R of the waveguide will vary in the different examples presented in this chapter from a

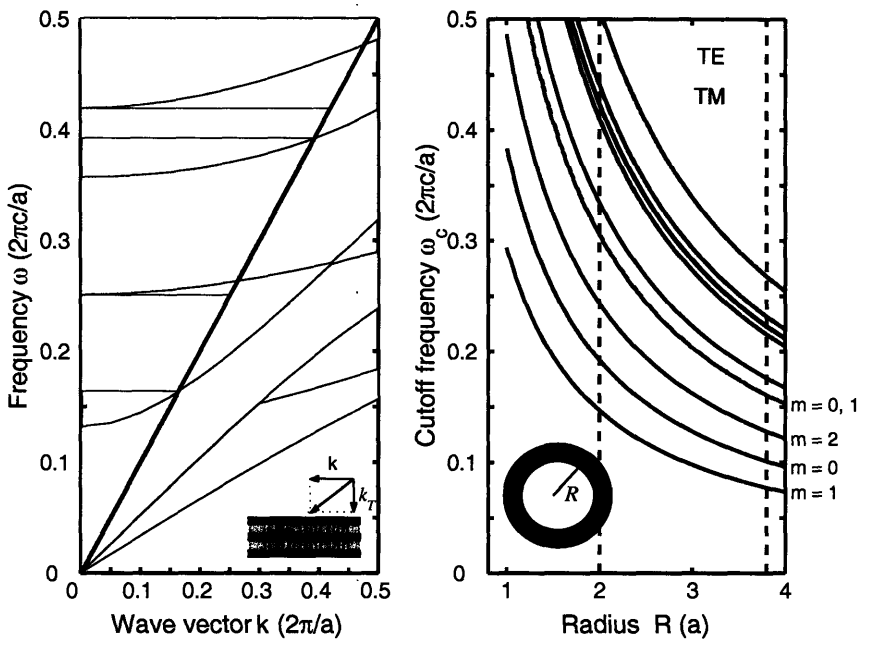

Figure 2-2: (Left) Projected band structure associated with the dielectric mirror. The blue regions correspond to (k, ω) pairs for which light can propagate through the mirror. The meaning of the parallel wave vector k is shown in the inset. k_T is the transverse component of the wave vector. The diagonal black line represents the light line ($\omega = ck$). Shown in gray are two frequency ranges corresponding to omnidirectional reflectivity of the mirror. (Right) Frequency cutoffs of the lowest 11 modes supported by a hollow metallic waveguide are plotted versus the radius of the waveguide. TE polarized modes are shown in red, while TM modes are shown in blue. The number m in the labels is the angular momentum index of each mode. Note the degeneracy of the TE_{01} and the TM_{11} modes. The two thick vertical dashed lines correspond to radii $R = 2.0a$ and $R = 3.8a$, which are the values used for the two exemplary waveguides considered here.

minimum of $2a$ to a maximum of $20a$.

On the right side of Fig. 2-1, we show a hollow metal waveguide. The core is the same as in the OmniGuide fiber (index of refraction 1, radius R), but a perfectly conducting metal cylinder now replaces the multilayer cladding.

We expect the multilayer structure to confine light in the core of the waveguide in a frequency range that corresponds to the band gap of a planar multilayer mirror having the same parameters as those of the multilayer structure in the waveguide. Indeed, it is precisely in this band-gap region that we expect the mode structure of

the OmniGuide fiber to resemble that of a hollow metal waveguide.

In the left panel of Fig. 2-2, we plot the projected band structure for a planar multilayer dielectric mirror for which the layers have the same indices of refraction and the same thicknesses as those of the layers present in the waveguide. If ω is the angular frequency of an incoming plane wave and k is the component of the wave vector parallel to the mirror, then regions in the (k, ω) plane shown in blue correspond to plane waves that can couple to propagating modes in the mirror and are transmitted through the mirror. The two gray areas in the plot correspond to the omnidirectional frequency ranges of the dielectric mirror. For these frequencies, light cannot be transmitted through the mirror for any angle of incidence of a plane wave incoming from the outside air region. Both the TE and TM polarizations are overlapped in the plot.

In the right panel of Fig. 2-2, the frequency cutoffs of the lowest 11 modes supported by a hollow metallic waveguide are plotted versus the radius of the waveguide. The dispersion relation of a mode with cutoff frequency ω_c is given by $\omega^2 = c^2k^2 + \omega_c^2$. TE polarized modes are shown in red, while TM modes are shown in blue. The number m in the labels is the "angular momentum" and describes the azimuthal symmetry of each mode. Note the degeneracy of the TE_{01} and the TM_{11} modes ($4th$ and $5th$ modes).

2.3 Calculation of Modes of the OmniGuide fiber

We calculate the modes supported by the OmniGuide fiber using the transfer-matrix method. As in any waveguide with cylindrical symmetry, there are three useful conserved quantities: ω, the frequency, k, the wave vector in the axial direction, and m, the angular momentum ($m = 0, 1, 2, \ldots$). The general form of the z component of the electric field, E_z, in the i-th layer of the structure for a mode with wave vector k

and angular momentum m is:

$$E_z(z,\, r,\, \phi) = [A_i \cdot J_m(k_{T,i}r) + B_i \cdot Y_m(k_{T,i}r)] \cdot \cdot e^{i(kz-\omega t)} e^{im\phi}, \tag{2.1}$$

where A_i and B_i are coefficients that vary from layer to layer, J and Y are Bessel functions, and $k_{T,i}$ is the transverse wave vector, $k_{T,i} = \sqrt{(n_i\omega/c)^2 - k^2}$. H_z is given by a similar expression, but with different coefficients C_i and D_i. From the E_z and H_z components one can calculate all the other components of the electromagnetic field components [27]. The coefficients in the $(i+1)$th layer are related to those in the i-th layer by a 4-by-4 transfer matrix, such that the boundary conditions are satisfied [13]. The last step before finding the modes is to establish boundary conditions at the outside surface of the outermost layer. Here we require that the incoming radial electromagnetic flux be zero, which corresponds to the physical situation in which the sources of electromagnetic field are only inside the waveguide [12]. The solutions that we obtain with this boundary condition are guided modes (with real wave vectors) and leaky modes (with complex wave vectors).

The OmniGuide fiber supports modes that are analogous to the guided modes of a hollow metallic waveguide. These modes are resonant modes that have most of their energy traveling in the hollow core. Their field decays exponentially in the radial direction in the dielectric layers. These modes have $(k,\, \omega)$ pairs situated in the band gap of the dielectric mirror and above the light line. The wave vector k has an imaginary part that is proportional to the radiative loss of the modes. This imaginary part decreases exponentially with the number of layers in the dielectric mirror; in the limit of an infinite number of layers these resonant modes become truly guided modes. For the dielectric mirror with only five layers shown in Fig. 2-1, the imaginary part is on the order of $10^{-4} \cdot 2\pi/a$. This means that light can be confined in the hollow core for a distance equal to several hundred wavelengths before it radiates

away. For a waveguide intended for transmission of light over longer distances, more layers need to be added to the cladding. Fortunately, the imaginary part of the wave vector decreases exponentially with the increase in the number of layers. Thus, for pure TE modes, only 20 layers are enough to give radiative decay lengths of more than a hundred kilometers, while for TM modes and mixed modes, 40 layers are enough. For a detailed analysis of radiation suppression see [23, 12].

The OmniGuide fiber also supports other categories of modes. One category includes modes that are index guided in the dielectric mirror. In Fig. 2-2, these modes are situated below the light line, in the light-blue regions of the $\omega(k)$ diagram. Their field decays exponentially in the air regions, but extends throughout the dielectric mirror. Another category includes modes that decay both in the air regions and in the dielectric layers. These only exist as surface states between the core and the multilayer cladding. (They can also be found deeper into the multilayer structure if a defect is introduced by altering the thickness or the index of refraction of one or more layers). In Fig. 2-2, these modes are situated below the light line in the band gap of the dielectric mirror.

2.4 Comparison of OmniGuide Fiber Modes and Metal Waveguide Modes

In Fig. 2-3, we show the lowest-frequency resonant modes of the OmniGuide fiber for a radius $R = 2.0a$. TE modes and TE-like (HE) modes are shown as solid red lines, while TM and TM-like (EH) modes are shown as solid blue lines. The modes of a hollow metallic waveguide with the same radius are shown as dots. The Figure shows that, indeed, the dispersion relations of the OmniGuide fiber are very similar to those of the metallic waveguide, but the modes can now only exist in the TE or TM band gaps of the multilayer mirror. For example, the TM_{01} mode in the metallic

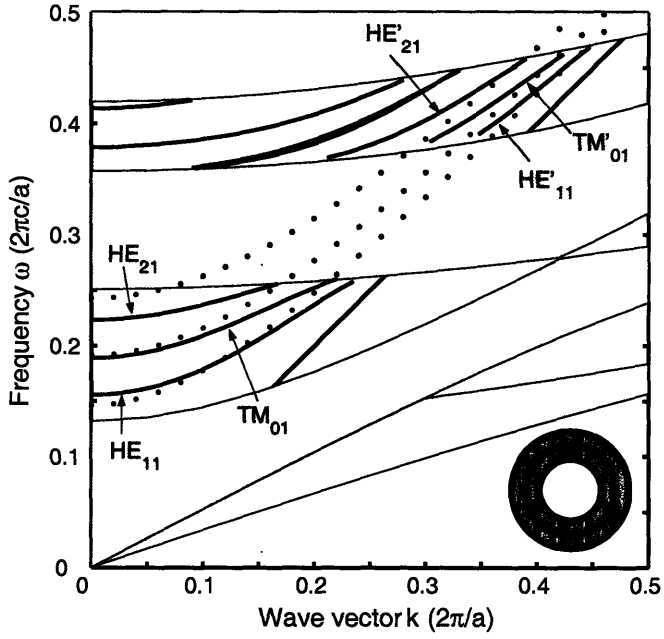

Figure 2-3: Modes supported by an OmniGuide fiber of radius $R = 2.0a$ are shown with solid lines. Red is for TE and HE modes, while blue is for TM and EH modes. Only the first three modes are labeled in each band gap. The lowest three modes in a hollow metallic waveguide with the same radius are plotted as dots.

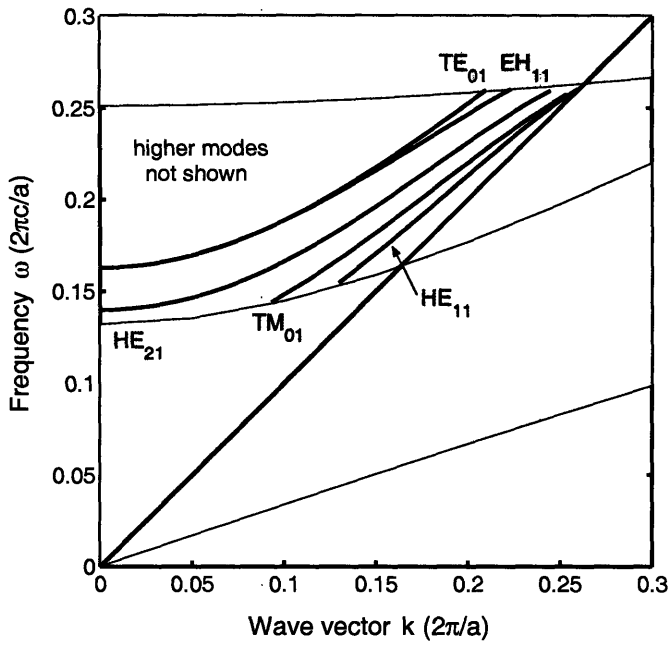

Figure 2-4: The lowest five modes supported by an OmniGuide fiber of radius $R = 3.8a$ are shown as solid red (TE or TE-like modes) and blue (TM or TM-like modes) curves. Higher modes exist, but are not shown.

waveguide (blue dots) is now split into two sub-modes, TM_{01} and TM'_{01}. Thus, it is useful, in a zeroth order approximation, to think that the dispersion relations for the different modes of the OmniGuide fibers can be obtained by overlapping the band structure of the dielectric mirror on top of the dispersion relations for the metallic waveguide. Finally, we note that it is possible for resonant modes to exist outside the omnidirectional frequency range (such as the HE_{11} mode for $k < 0.05\,(2\pi/a)$ in Fig. 2-3) as long as the modes fall within the band gap.

In Fig. 2-4, we show the dispersion relations for a larger radius of the fiber, $R = 3.8a$. More resonant modes can be found now in the first band gap, as the cutoff frequencies vary inversely with the radius R. We focus on the first band gap of the dielectric mirror, and we consider only the lowest five resonant modes of the waveguide.

We will compare the resonant modes shown in Fig. 2-3 and Fig. 2-4 with the modes

Mode label		Cutoff frequency			Degeneracy	
OGF	HMW	OGF	HMW	Diff.	OGF	HMW
HE_{11}	TE_{11}	0.155	0.146	+6%	2	2
TM_{01}	TM_{01}	0.189	0.191	-1%	1	1
HE_{21}	TE_{21}	0.223	0.243	-8%	2	2
EH_{11}	TM_{11}	0.163	0.160	+2%	2	2
TE_{01}	TE_{01}	0.163	0.160	+2%	1	1

Table 2.1: Summary of comparison between OmniGuide fiber (OGF) modes and their hollow metallic waveguide (HMW) counterparts. The first three modes are taken from Fig. 3 for a radius $R = 2.0a$, and the next two are from Fig. 4, corresponding to $R = 3.8a$.

in metal waveguides of corresponding radii ($R = 2.0a$ and $R = 3.8a$). In particular, we will compare the resonant modes to the metal waveguide modes in terms of their cut-off frequencies, group velocities, group velocity dispersions, degeneracies and mode symmetries. The lowest resonant mode in Fig. 2-3 is HE_{11}, with a cutoff frequency $\omega = 0.155\,(2\pi/a)$. This corresponds to TE_{11}, the fundamental mode in a hollow metal waveguide, which has a cutoff at $\omega = 0.146\,(2\pi/a)$. The second mode in Fig. 2-3 is TM_{01} with $\omega = 0.189\,(2\pi/a)$, corresponding to TM_{01} in the metal waveguide with $\omega = 0.191\,(2\pi/a)$. Note that for $m = 0$ modes, the OmniGuide fiber modes are exactly TE or TM polarized, as is the case with all metal waveguide modes. For non-zero m, TE modes become HE modes, and TM modes become EH modes. Also, in both waveguides, the non-zero m modes are doubly degenerate, while the $m = 0$ are non-degenerate.

In Table 1, we summarize the similarities between the equivalent modes in the OmniGuide fiber and the hollow metallic waveguide. The first three modes are taken from Fig. 2-3 for a radius $R = 2.0a$, and the next two are from Fig. 2-4, corresponding to $R = 3.8a$. The cutoff frequencies for the two types of waveguides are quite similar for all the five modes. The differences vary from -8% for the HE_{21} mode, to +6% for the TM_{01} mode. Note also that modes that in the metal waveguide have low cutoff frequencies (below $0.18\,(2\pi/a)$) are shifted up in the OmniGuide fiber, while metallic

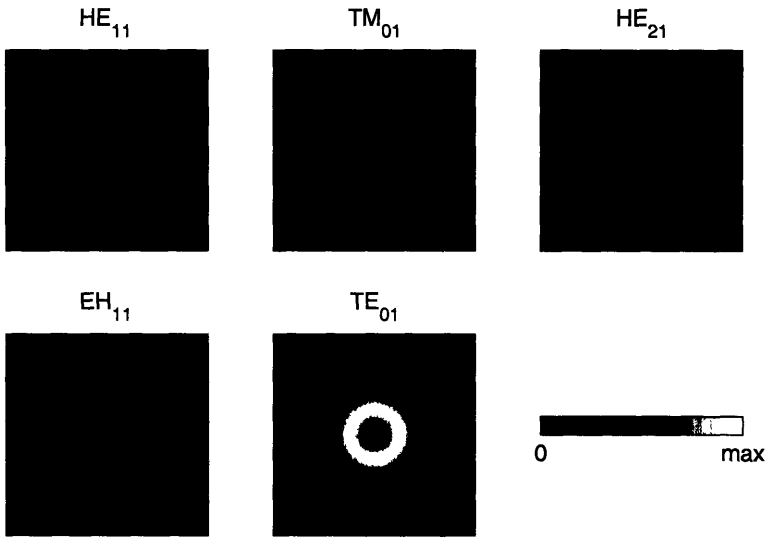

Figure 2-5: The electric-field time-average energy density for the five modes in Fig. 4 is shown in a transverse cross section of the waveguide. The color scheme is such that the energy density goes from zero (black) to maximum (yellow). The thin blue contours represent the contours between the different layers of the OmniGuide fiber. For all five modes, the energy density is plotted for a frequency $\omega = 0.230\,(2\pi/a)$.

modes with higher cutoff frequencies are shifted down. This effect will be explained later in terms of the phase shift of the dielectric mirror.

The group velocity of a resonant mode is zero at $k = 0$ and approaches c as the frequency is increased, as is the case in a metal waveguide. However, as the mode nears the upper band edge, the group velocity starts decreasing as a result of the gradual loss of confinement in the core.

The group velocity dispersion of a resonant mode is positive for low frequencies (closer to the lower edge of the band gap), negative for high frequencies and transitions through zero. This is in contrast to the group velocity dispersion of modes in a metal waveguide, which is always positive.

To provide a better understanding of the field patterns of OmniGuide fiber modes, in Fig. 2-5 the electric-field time-average energy density $\frac{1}{2}\varepsilon \left|\vec{E}\right|^2$ is plotted for the five modes shown in Fig. 2-4 at a frequency $\omega = 0.230\,(2\pi/a)$. All modes are normalized such that the power flowing in the z direction is the same. Also, in order to capture

the angular dependence of a mode, we no longer use the $e^{im\phi}$ complex form of the field. Instead, we use linear combinations of the degenerate m and $-m$ modes to obtain real fields.

All modes appear to be very well confined to the hollow core. The energy density in the cladding layers is much smaller than the energy density in the core, which is why the cladding layers appear dark in the Figure. The TE_{01} mode is different from the other four modes in that its electric field energy density has a node near the core-mirror interface. This is true in general for all modes of the same symmetry, *i.e.* $TE_{0\ell}$ with $\ell = 1, 2, \ldots$. Note that the number of angular oscillations of the energy density is twice the angular momentum of a mode.

In order to quantify the comparison between the field distribution of modes in the OmniGuide fiber and in the metal waveguide we use a correlation function Γ defined by:

$$\Gamma = \frac{\left| \int r dr d\phi \vec{E}_1(r, \phi) \cdot \vec{E}_2(r, \phi) \right|}{\left[\int r dr d\phi \left| \vec{E}_1(r, \phi) \right|^2 \int r dr d\phi \left| \vec{E}_2(r, \phi) \right|^2 \right]^{1/2}} \tag{2.2}$$

Γ can take values in the interval [0, 1], a value of 1 corresponding to maximum correlation ($\Gamma = 1$ can only happen if the two modes are the same up to a constant amplitude scaling factor). For all modes, the correlation is largest close to the middle of the band gap and decreases as the mode approaches the band edges. The maximum value of the correlation as a function of frequency is above 95% for all modes, and the largest correlation is found for the TE_{01} mode: 99.1%.

2.5 Phase-Shift Model

In both the hollow metallic waveguide and the OmniGuide fiber, light is confined in the air region because it is reflected back to the core by a cladding: a metal wall in

the first case and a dielectric multilayer film in the second. Thus, it is convenient to analyze the differences between the modes in the two waveguides in terms of the different reflection properties of the two mirrors. Since the reflectivity is very close to 100% in both cases, the important difference between the two mirrors is found in the phase shift $\Delta\phi$ acquired by an electromagnetic wave upon reflection. For the TE polarization, this phase shift is defined by:

$$\frac{E_r^{||}}{E_i^{||}} = e^{i\Delta\phi}, \tag{2.3}$$

where $E_i^{||}$ and $E_r^{||}$ are the tangential components of the electric field for the incident and reflected waves respectively. In the above formula, we assume that the reflectivity is 100%, which is true for a perfectly conducting wall and is a very good approximation for a dielectric mirror with a large enough number of layers. For a metallic mirror, $\Delta\phi$ is always equal to π because the tangential electric fields of the incident and reflected waves have to cancel. For the TM polarization we calculate $\Delta\phi$ in a similar manner, using the tangential components of the magnetic field this time: $H_r^{||}/H_i^{||} = -e^{i\Delta\phi}$. With this definition, $\Delta\phi$ for a metal mirror is equal to π for all polarizations and angles of incidence.

In Fig. 2-6 we plot the phase shift of the dielectric mirror as contours on a plot which includes the band gap edges, the light line, and dispersion relations for the fiber with $R = 2.0a$. The phase shift is a function of ω and k, or, equivalently, of the frequency and the angle of incidence. Also, it is a function of the polarization of the incident wave. For both polarizations, we can identify a $\Delta\phi = \pi$ line near the center of the band gap (shown with a thicker black line). This is where we expect the dielectric mirror to be most similar to a metal mirror. The other contour lines correspond to phase shifts of 1.1π, 1.2π,... for increasing frequencies, and 0.9π, 0.8π,... for decreasing frequencies. The qualitative difference between the two polarizations is that for the TE polarization the phase shift at a given frequency approaches π near

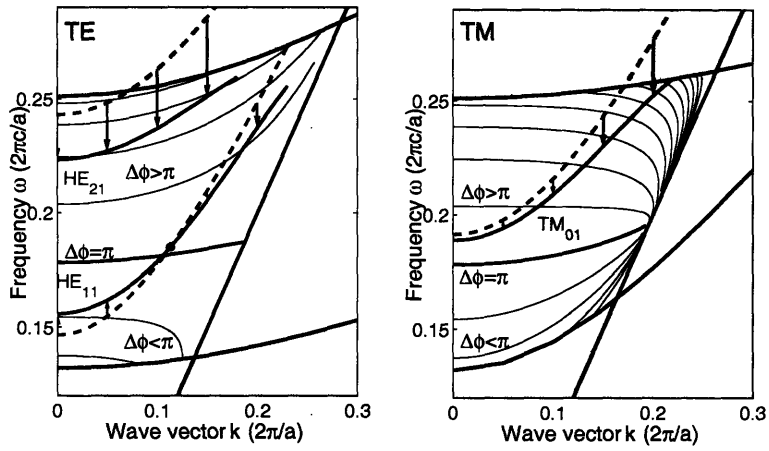

Figure 2-6: Combined phase shift and dispersion relation diagrams. Left panel: contour lines for the phase shift, $\Delta\phi$, are plotted together with the band gap of the dielectric mirror (white region), and the light line (black oblique line). The modes of the OmniGuide fiber with $R = 2.0a$ are shown as solid red/blue lines for TE/TM-like modes, while the modes in the metal waveguide are showed as dotted lines. The vertical arrows show the frequency difference between equivalent modes in the waveguides. The left and right panels are for modes with TE-like and TM-like polarization, respectively. The crossing between the OmniGuide HE_{11} mode and the metallic TE_{11} mode is shown as a black dot.

the light line, whereas for the TM polarization it varies substantially near the light line.

Also shown in Fig. 2-6 are the confined modes for the metallic waveguide (dashed lines) and for the OmniGuide fiber (solid lines). On the left, we present TE-like modes while on the right the pure TM mode is shown.

As seen in Fig. 2-6, the difference in the dispersion curves for the confined modes in the metallic waveguide and the OmniGuide fiber are correlated with the difference in phase shifts between the dielectric and metal mirrors. In particular, the following observations can be made:

The point of crossing between the mode and the metallic TE_{11} mode lies very close to the $\Delta\phi = \pi$ line.

(*ii*) The frequency distance between the equivalent modes in the metal and dielectric waveguides increases as the phase shift of the dielectric mirror moves away

from $\Delta\phi = \pi$.

(*iii*) The confined modes in the dielectric waveguide are drawn towards the $\Delta\phi = \pi$ line when compared with the modes confined in the metal waveguide.

Next we present a simple model that explains qualitatively the above observations by relating the phase shift to the dispersion curves. We approximate the transverse field profile of a confined mode of the OmniGuide fiber by a standing wave between two planar walls separated by the diameter of the waveguide. The total phase acquired by a wave that traverses the waveguide diameter twice has contributions from propagation over a distance $2 \cdot (2R)$ and from two reflections upon the mirror. Thus,

$$\Delta\phi_{total} = 4k_T R + 2\Delta\phi, \tag{2.4}$$

where k_T is the transverse wave vector of the mode in core. The condition for a standing wave is that this phase must equal a multiple of 2π: $\Delta\phi_{total} = 2\ell\pi$. This in turn leads to the approximate dependence of the transverse wave vector on the phase shift:

$$k_T = (\ell\pi - \Delta\phi)/(2R). \tag{2.5}$$

Calculating k_T from this equation should be done self-consistently because $\Delta\phi$ is a function of ω and k, and therefore a function of k_T.

From Eq. (2.5) we see why the phase shift $\Delta\phi$ has important effects on the dispersion relations of modes. Since k_T is a decreasing function of $\Delta\phi$, and because $\omega^2/c^2 = k^2 + k_T^2$, it follows that an increase in the phase shift $\Delta\phi$ will cause a decrease of the frequency ω of a mode at a fixed wave vector k. This result explains the three qualitative observations made above about the OmniGuide modes when compared to the metallic waveguide modes.

The most important and visible difference between the two sets of modes is that

the OmniGuide modes are pulled inside the band gap when compared to their metallic counterparts. This is entirely due to the fact that the phase shift increases with increasing frequency. One consequence is that the group velocity of the OmniGuide modes is always slightly smaller than that of the corresponding metallic modes. It is interesting to imagine what would happen if one could design a multilayer dielectric mirror for which the phase shift decreased with increasing frequency: in such a waveguide, the modes would be pulled out towards the band-gap edges, leading to modes with larger group velocities which could approach the upper bound of c. However, it is an empirical law that the phase shift always has the general behavior shown in Fig. 2-6. Finally, we note that the point of maximum correlation between OmniGuide fiber modes and metallic modes, as defined above, occurs very close to the $\Delta\phi = \pi$ line.

2.6 Special Characteristics of the TE_{01} Mode

For practical applications, it is of interest to identify the losses associated with the different modes of the waveguide. Metallic waveguides were the subject of intensive research aimed at utilizing them for long distance optical communications. It was found that the TE_{01} mode is the lowest loss mode in a metal waveguide, due to the presence of a node in the electric field at the metallic wall. This mode was the operating mode for the long distance communication lines designed by the Bell Laboratories prior to the advent of silica fibers [9]. In the remaining portion of chapter, we will examine some of the properties of the TE_{01} mode in the OmniGuide fiber; these properties were studied in more detail in [12].

In the left panel of Fig. 2-7, we plot the confinement in percent of the electromagnetic energy in the core for the TE_{01}, TM_{01}, and HE_{11} modes as a function of the core radius for a fixed frequency, $\omega = 0.256\,(2\pi/a)$. As shown, the TE_{01} mode has

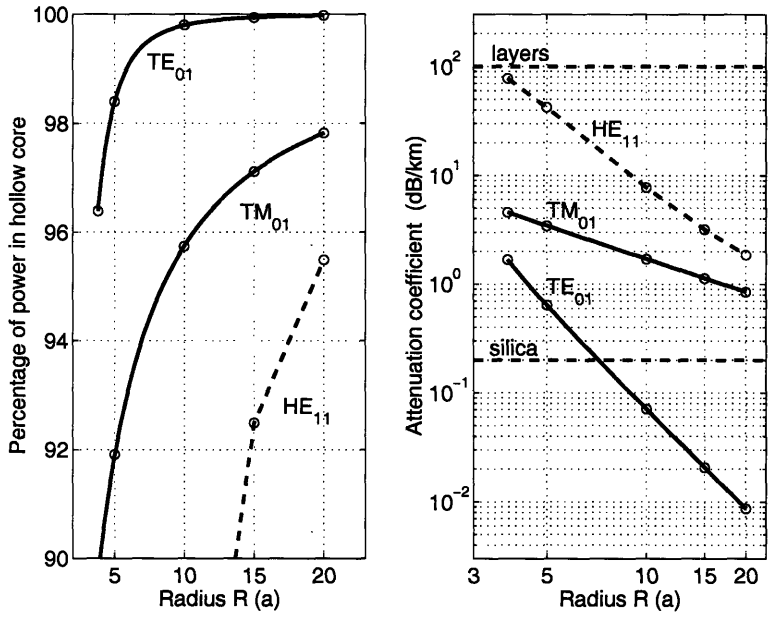

Figure 2-7: (Left) The confinement of electromagnetic energy in the hollow core of the OmniGuide fiber is plotted for three modes as a function of core radius. Actual data is shown as open circles. The solid lines represent fits as discussed in the text, and the dashed line is simply connecting the data points. (Right) The attenuation coefficient of the three modes is plotted as a function of radius. Also shown are the attenuation coefficient in silica fibers (0.2 dB/km) and a much larger attenuation coefficient (100 dB/km) assumed for the materials in the multilayer mirror. The circles and the lines have the same significance as in the left panel.

the largest confinement for all values of R. Furthermore, its confinement in the core approaches 100% at a faster rate then the other modes. The penetration of the TE_{01} field into the multilayer structure is very well approximated by a $1/R^3$ dependence. We will present a justification for the $1/R^3$ dependence below. A fit to the actual data points (open circles) is shown in Fig. 2-7 as a solid red line. The TM_{01} confinement approaches 100% at a much lower rate. A fit with a $1/R^3$ dependence is shown as a solid blue line. The HE_{11} mode has a mixed polarization and has a more complex variation with the core radius. However, the rate at which its confinement approaches 100% is less than that of the TE_{01} mode.

In the right panel of Fig. 2-7, we plot the attenuation coefficient caused by dissipation losses for the three modes. (We assume the dielectric mirror has enough layers such that the radiation losses are negligible). We assume the core of the waveguide is lossless, while the materials in the dielectric mirror have a dissipation coefficient of 100 dB/km (chosen to much larger than the loss of silica). Even with such lossy materials in the dielectric mirror, the loss of the TE_{01} mode is smaller than the loss of silica fibers (0.2 dB/km) if the core radius R is larger than approximately $8a$. This is because the dissipation loss for $TE_{0\ell}$ ($\ell = 1, 2, \ldots$) modes decreases as $1/R^3$. This general result is a consequence of the presence of a node in the electric field near the core-mirror interface, as will be shown below. Note that while the silica fiber has a very low loss only for wavelengths near $\lambda = 1.55\mu m$, the OmniGuide fiber can be designed to have a very low loss in the vicinity of any desired wavelength, from infrared to visible wavelengths.

The $1/R^3$ dependence of the TE_{01} dissipation loss is due to the presence of a node in the electric field of this mode near the interface between the hollow core and the first layer of the dielectric mirror. The only non-zero component of the electric field for the TE_{01} mode is E_ϕ. In the case of a metallic waveguide, this component would be exactly zero at the interface between the hollow core and the metal. In the case

of the dielectric waveguide, the node in E_ϕ is found very close to the interface.

To get an estimate of the dissipation losses, we take the ratio of the power that travels in the layers to the total power carried by the mode. A more precise expression is derived in [12], but the proof of the $1/R^3$ dependence is the same. Let A_{core} be the amplitude of the electric field in the core, and A_{layers} the amplitude in the layers. The area of the core is πR^2. Because of the exponential radial decay induced by the band gap, the power in the layers is found mostly in the first few layers, in an area approximately equal to $2\pi R \cdot d_p$ (d_p is the penetration depth of the field into the layers and is independent of R). With these notations, the estimate for the loss coefficient is:

$$\text{Loss} \sim \frac{A_{layers}^2 \cdot 2\pi R d_p}{A_{core}^2 \cdot \pi R^2} \sim \frac{1}{R} \cdot \left(\frac{A_{layers}}{A_{core}}\right)^2 \tag{2.6}$$

where we kept only terms that influence the R dependence.

Because of the small amplitude of E_ϕ at the core-layers interface, it is the derivative of E_ϕ with respect to r that connects the amplitudes A_{layers} and A_{core}. If we approximate the radial field oscillations by sinusoidal oscillations, the derivative of E_ϕ close to a node is given by the transverse wave vector times the amplitude of E_ϕ. Thus, the amplitudes in the core and in the layers are connected by $k_{T,core}A_{core} \simeq k_{T,layers}A_{T,layers}$. The transverse wave vector $k_{T,core}$ is inversely proportional to R, because the TE_{01} mode always has half an oscillation of E_ϕ between the origin and $r = R$. In a layer with index of refraction n, we have $k_T = \sqrt{(n\omega/c)^2 - k^2}$. As R becomes larger, the TE_{01} mode will get closer to the light line, and therefore k approaches ω/c. If n is not equal to 1, k_T will be almost independent of R. Thus $k_{T,layers}$ is almost independent of R. Thus, we have

$$\frac{A_{layers}}{A_{core}} \simeq \frac{k_{T,core}}{k_{T,layers}} \sim \frac{1}{R}. \tag{2.7}$$

The expression for the loss becomes:

$$\text{Loss} \sim \frac{1}{R} \cdot \left(\frac{A_{layers}}{A_{core}} \right)^2 \sim \frac{1}{R^3}, \tag{2.8}$$

which is the result we wanted to justify.

TE_{01} is the lowest loss mode within the $TE_{0\ell}$ family of modes. From the derivation above one can show that the loss of a $TE_{0\ell}$ mode is proportional to the square of the transverse wave vector in the core, $k_{T,core}$. This implies a monotonic increase of the loss with the order ℓ. In particular the loss of TE_{02} is about 3.3 times larger than that of TE_{01} for almost all frequencies and core radii.

For modes other than the $TE_{0\ell}$ modes, the absence of the node in the electric field near the core-layers interface results in more penetration of the field into the cladding, and also different scaling laws for the R dependence. Turning back to Fig. 2-7, we see that the TM_{01} dissipation loss follows exactly a $1/R$ dependence (solid blue line), while the loss of HE_{11} has some intermediate dependence, with a slope that approaches $1/R$ for large R.

Another reason for the low losses of the TE_{01} mode is the fact that this mode is confined in the core only by the TE gap. TM modes and mixed modes have a component that is confined by the weaker TM gap, and thus they penetrate deeper into the multilayer cladding.

The fact that the TE_{01} loss is smaller than that of the other modes is very important for the transmission properties of OmniGuide fibers. Even if several modes are excited at the input of a waveguide, after a certain distance only the TE_{01} mode will remain in the waveguide. This loss-induced modal discrimination results in an effectively single-mode operation in a waveguide that supports many modes. In our analysis, we assumed that the number of layers in the dielectric mirror is large enough such that radiation losses can be neglected. By choosing the number of layers ap-

propriately, the loss-induced modal discrimination can be further enhanced since the radiation losses are also smallest for TE_{01} [13, 16, 12].

While the radiation and absorption losses of the TE_{01} decrease substantially when the core radius is increased, the analysis of attenuation in a practical waveguide necessitates the consideration of other loss mechanisms. In particular, the loss of the TE_{01} mode is increased by coupling to other resonant modes or to cladding modes due to deviations from a straight and perfect waveguide. These effects are analyzed in detail in [12].

2.7 Recent Experimental Developments

Recently, there has been great interest in implementing these hollow-core fiber designs in practice, because they offer the potential to minimize the dependence of light transmission properties on fiber material characteristics such as losses and nonlinearities. It turns out that the easiest way to manufacture the multilayered mirror cladding is by rolling a bilayer (one high-index layer and one low-index layer) sheet around a central rod, thus creating a spiraled layered structure [28]. The central rod is then removed to obtain a large-radius hollow-core multilayered preform which is subsequently heated and drawn into fiber. The fiber in Ref. [28] was made of a chalcogenide glass with $n = 2.8$ and a polymer with $n = 1.55$, thus having a smaller index contrast than the one used in our work. The core radius was about $350\,\mu$m and the bilayer thickness $3.5\,\mu$m, resulting in a R/a ratio of about 100. Even in a multi-mode transmission regime, the fiber achieved a loss of less than 1 dB/m at $10.6\,\mu$m, orders of magnitude lower than the loss of the polymer layers in the cladding which is about $100,000$ dB/m. The spiraled structure of the fiber includes a seam at the interface between the hollow core and the dielectric mirror. This defect should increase the losses of the fiber, but the contribution is expected to be small at large radii (for the

TE_{01} mode a $1/R^4$ scaling of the extra loss is predicted from perturbation theory).

2.8 Conclusions

We have analyzed in this chapter the electromagnetic mode structure of an OmniGuide fiber – a hollow dielectric waveguide in which light is confined by a large index-contrast omnidirectional dielectric mirror. The modes in such a fiber are similar to those in a hollow metallic waveguide in their symmetries, cutoff frequencies and dispersion relations and we have shown that the differences can be predicted by a model based on a single parameter - the phase shift upon reflection from the dielectric mirror. The analogy to the metal waveguide extends to the transmission properties, resulting in the identification of the TE_{01} mode as the lowest loss mode of the hollow-core photonic band gap fiber. It is hoped that the analogy developed here has provided an intuitive understanding of the modal structure of the OmniGuide fiber and could be applied to the design of transmission lines or optical devices based on this type of fiber.

Chapter 3

An All-Dielectric Coaxial Waveguide

Preface

This chapter is based on Ref. [25]: M. Ibanescu, Y. Fink, S. Fan, E. L. Thomas, and J. D. Joannopoulos, "An all-dielectric coaxial waveguide," *Science*, vol. 289, p. 415–419 (2000). In addition to the material already covered in the article, we also present here more recent developments and analyses. In section 3.4 we discuss differences between coaxial omniguide modes and their traditional coaxial waveguide modes based on a simple phase shift model. In section 3.5 we expanded the part about dispersionless propagation at a special frequency inside the single-mode frequency window, and we also comment on the flatness of the $m = 1$ band in Fig. 3-4 and relate it to the unusual dispersion relations of Chapter 4.

3.1 Introduction

Waveguides are the backbone of modern optoelectronics and telecommunications systems. There are currently two major, and very distinct, types of waveguides (metallic and dielectric) that are used in two separate regimes of the electromagnetic spectrum. For microwave and radio frequencies, the metallic coaxial cable is of greatest promi-

nence [29]. In this type of cable, the entire electromagnetic field is confined between two coaxial metal cylinders. The important fundamental electromagnetic mode of a coaxial cable is the transverse electromagnetic (TEM) mode, which is unique in that it has radial symmetry in the electric field distribution and a linear relationship between frequency and wave vector. This gives the TEM mode two exceptional properties. First, the radial symmetry implies that one need not worry about possible rotations of the polarization of the field after it passes through the waveguide. Second, the linear relationship ensures that a pulse of different frequencies will retain its shape as it propagates along the waveguide. The crucial disadvantage of a coaxial metallic waveguide is that it is useless at optical wavelengths because of heavy absorption losses in the metal. For this reason, optical waveguiding is restricted to the use of dielectric materials. However, because of the differences in boundary conditions of the electromagnetic fields at metal and dielectric surfaces, it has not previously been possible to recreate a TEM-like mode with all-dielectric materials.

Consequently, optical waveguiding is done with the traditional index-guiding (that is, total internal reflection) mechanism, as exemplified by silica and chalcogenide optical fibers. Such dielectric waveguides can achieve very low losses [30]. Although the optical fiber has proven to be undeniably successful in many ways, it is nevertheless plagued by two fundamental problems. First, because the fundamental mode in the fiber has an electric field with twofold p-like symmetry, the polarization of light coming in one end of the fiber and the polarization coming out the other are generally completely different. This leads to substantial problems when coupling into polarization-dependent devices. Second, because the guiding involves total internal reflection, it is not possible for light to travel in a fiber with a sharp bend whose radius of curvature is less than 3 mm without significant scattering losses [31]. For light at optical wavelengths, this is a gcomparatively enormous radius, thus limiting the scale of possible miniaturization.

Recently, however, all-dielectric waveguides have been introduced that confine optical light by means of one-dimensional [21] and two-dimensional [32, 33] photonic bandgaps. These new designs have the potential advantage that light propagates mainly through the empty core of a hollow waveguide [12, 13], thus minimizing effects associated with material nonlinearities and absorption losses[1]. Moreover, because confinement is provided by the presence of at least a partial photonic bandgap, this ensures that light should be able to be transmitted around a bend with a smaller radius of curvature than is possible with the optical fiber.

Here we introduce a waveguide, the coaxial omniguide, that combines some of the best features of the metallic coaxial cable and the dielectric waveguides. It is an all-dielectric coaxial waveguide and supports a fundamental mode that is very similar to the TEM mode of the metallic coaxial cable. It has a radially symmetric electric field distribution so that the polarization is maintained throughout propagation. It can be designed to be single-mode over a wide range of frequencies. In addition, the mode has a point of intrinsic zero dispersion around which a pulse can retain its shape during propagation, and this point of zero dispersion can be placed in the single-mode frequency window. Finally, the coaxial omniguide can be used to guide light around sharp bends whose radius of curvature can be as small as the wavelength of the light. This waveguide design is completely general and holds over a wide range of structural parameters, materials, and wavelengths. To our knowledge, this work represents the first successful attempt to bridge the disparate modal regimes of the metallic coaxial cable and the dielectric waveguides.

[1]The first attempts at hollow waveguides in the optical regime actually involved metallodielectric materials. See for example Ref. [34].

3.2 From Metallic to All-Dielectric Waveguides

A cross section of a traditional metallic coaxial waveguide is shown in Fig. 3-1(a). Light is confined in the radial direction in the region between the two metal cylinders and travels in the axial direction (perpendicular to the plane of the figure). In a simple ray model, propagation of light through the coaxial cable can be viewed as a result of successive specular reflections off the metal walls. The dispersion relations for the first few modes supported by a metallic coaxial waveguide are shown in Fig. 3-2(a). For definiteness, the inner and outer radii of the waveguiding region are taken to be $r_i = 3.00a$ and $r_o = 4.67a$, respectively, where a is an arbitrary unit of length to be defined later. For any value of the wave vector, the lowest frequency mode is the TEM mode for which both the electric and magnetic fields are transverse to the direction of propagation. This mode has zero angular momentum, which means that the mode is invariant under rotations around the axial direction. Another useful property of this mode is its constant group velocity, which makes it dispersionless at any frequency. The other modes shown in the plot are transverse electric (TE_{ml}) modes for $l = 1$ and varying angular momenta m. The cutoff frequency of any of these modes is of the form

$$\omega_{\text{cutoff}} = \frac{c}{r_o} f\left(\frac{r_o}{r_i}\right)$$

where f is the solution to a transcendental equation for each value of the angular momentum m [29]. The waveguide also supports transverse magnetic (TM) modes, but they do not appear in the plot because the cutoff frequency for the lowest lying TM mode is larger than $0.30\,(2\pi c/a)$.

Designing an all-dielectric waveguide with similar principles of operation as the metallic coaxial waveguide is not straightforward, because the boundary conditions at a dielectric-dielectric interface differ from those at an air (dielectric)-metal interface. In particular, specular reflections cannot be obtained on a dielectric-dielectric

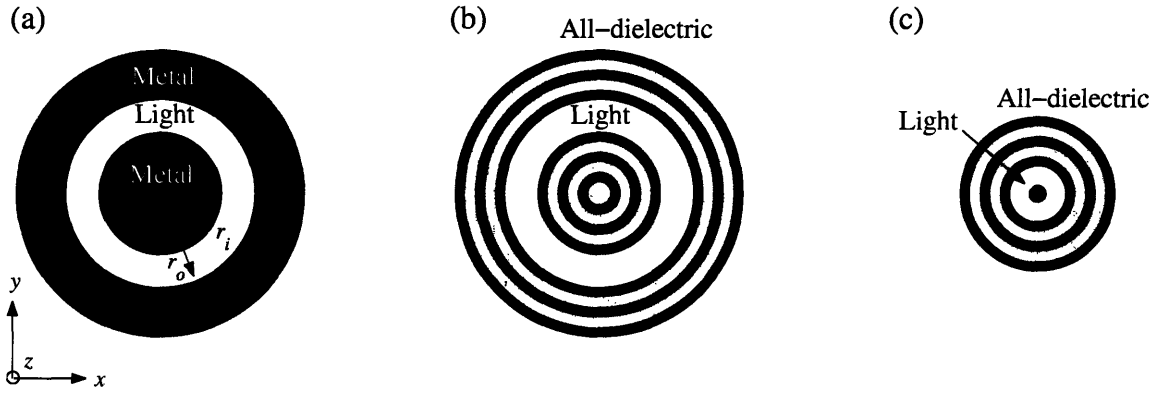

Figure 3-1: Schematics of coaxial waveguide cross sections: (a) traditional metallic coaxial cable; (b) coaxial omniguide, type A; and (c) coaxial omniguide, type B. In parts (b) and (c), the gray layers represent cylindric dielectric layers, with dark gray corresponding to the high dielectric constant material, and the light gray corresponding to the low dielectric constant material. For all cases (a–c), light can be confined within the coaxial region, shown in yellow, and guided along the axial z-direction. In (a) and (b) the inner and outer radii of the coaxial region are $r_i = 3.00a$ and $r_o = 4.67a$, whereas in (c) $r_i = 0.40a$ and $r_o = 1.40a$.

interface when the ray of light comes from the region with a lower index of refraction. Thus, it has generally been assumed that an all-dielectric coaxial waveguide cannot be designed to support a TEM-like mode, even in principle. However, recent research on the omnidirectional dielectric reflector has opened new possibilities for reflecting, confining, and guiding light with all-dielectric materials [18]. Indeed, a dielectric hollow waveguide using this principle was recently fabricated and tested successfully at optical wavelengths (4). The omnidirectional dielectric reflector, or simply the dielectric mirror, is a periodic, multilayered planar structure consisting of alternating layers of low and high indices of refraction. This structure can be designed so that there is a range of frequencies at which incoming light from any direction and of any polarization is reflected. Moreover, the electric fields of the reflected light in this frequency range have corresponding phase shifts that are quite close to those acquired upon reflection from a metal. In fact, there is a frequency for each angle of incidence and each polarization, for which the phase shift is identical to that of a metal. This

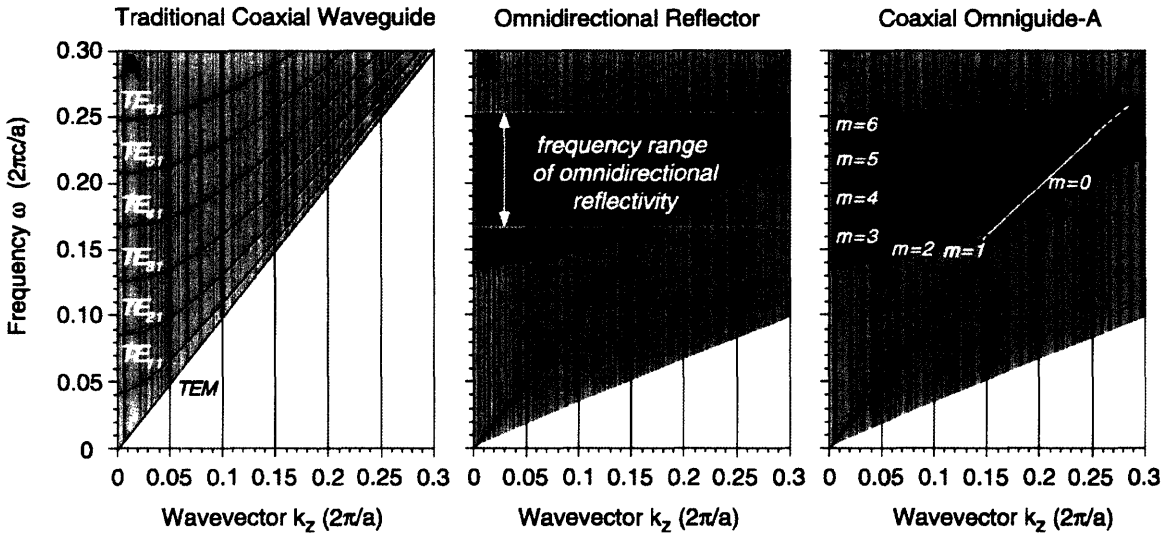

Figure 3-2: Projected band structures along an axial direction. (a) Traditional metallic coaxial cable with inner and outer coaxial radii of $r_i = 3.00a$ and $r_o = 4.67a$, respectively. The red bands correspond to allowed guided modes. For any given wavevector, the lowest frequency mode is a TEM mode characterized by a perfectly linear dispersion relation. The six next highest bands correspond to transverse electric (TE_{ml}) modes with $l = 1$ and increasing angular momentum m. (b) Omnidirectional, reflecting, all-dielectric multilayer film. Light-blue regions correspond to modes for which light is allowed to propagate within the dielectric mirror, and dark-blue regions correspond to modes for which light is forbidden to propagate within the dielectric mirror. The diagonal black line identifies the edge of the light cone. The horizontal gray lines mark the boundaries in frequency within which omnidirectional reflectivity is possible. (c) Coaxial omniguide A with inner and outer coaxial radii of $r_i = 3.00a$ and $r_o = 4.67a$, respectively, and bilayers consisting of indexes of refraction $n_1 = 4.6$ and $n_2 = 1.6$ and thickness $d_1 = 0.33a$ and $d_2 = 0.67a$, respectively. The red and yellow bands indicate guided modes confined to the coaxial region of the waveguide. The dashed lines indicate modes with less than 20% localization within the coaxial region. There is close correspondence between the modes labeled $m = 1$ to $m = 6$ and those of part (a) labeled TE_{11} to TE_{61}. Also, the yellow $m = 0$ mode corresponds to a TEM-like mode, as discussed in the text.

observation, together with the fact that high reflectivity of the omnidirectional dielectric mirror is maintained for all angles of incidence, strongly suggests exploration of the possibilities of using an omnidirectional mirror in lieu of a metal in coaxial cable designs. In effect, the omnidirectional dielectric mirror provides a new mechanism for guiding optical and infrared light without incurring the inherent losses of a metal.

In a cross section of a coaxial waveguide (Fig. 3-1(b)), the metal cylinders from the left panel have been replaced with cylindrical dielectric layers associated with an omnidirectional mirror. We call this particular coaxial waveguide embodiment coaxial omniguide A. The parameters of the dielectric layers are taken from the hollow waveguide experiment [21] to be the following: layers shown in dark gray have an index of refraction $n_1 = 4.6$ and a thickness $d_1 = 0.33a$, whereas layers shown in light gray have $n_2 = 1.6$ and $d_2 = 0.67a$. Here, $a = d_1 + d_2$ is the unit length of periodicity of the multilayered structure. The inner (r_i) and outer (r_o) radii of the coaxial waveguiding region are taken to be the same as those of the metallic coaxial cable described earlier. For the calculations presented here, we have set the index of refraction of the coaxial waveguiding region to be 1. In practice, in order to provide structural support, the coaxial waveguiding region may be chosen to be a dielectric with a low index of refraction without affecting the favorable properties of the coaxial omniguide. For example, setting the index of refraction of the coaxial waveguiding region to 1.3 (instead of 1.0), with $n_1 = 4.6$, $n_2 = 1.8$, the original omnidirectional reflectivity range of 0.17 to 0.25 $(2\pi c/a)$ in Fig. 3-2(b) reduces to a range of 0.18 to 0.23 $(2\pi c/a)$, whereas the modal structure shown in Fig. 3-2(c) remains essentially unaltered.

Before we begin our investigation of the modes supported by the coaxial omniguide, it is instructive to first review the modes of a planar omnidirectional dielectric mirror. The projected band structure of the omnidirectional mirror is shown in Fig. 3-2(b). The light blue regions represent allowed propagation modes of light within the

dielectric mirror. The dark blue region represents modes for which light is forbidden to propagate within the dielectric mirror. The thick black line identifies the edge of the light cone, and the horizontal gray lines demarcate the frequency range of omnidirectional reflectivity. It is precisely within this range of frequencies that one would expect the coaxial omniguide to support modes that are most reminiscent of those of the metallic coaxial cable.

3.3 Calculation of Coaxial Omniguide Modes

To calculate the frequencies and field patterns of the modes of coaxial omniguide A, we proceed as described below. As a result of the cylindrical symmetry of the system, there are two good "conserved quantities" that can be used to specify and classify the various modes supported by this waveguide. These are k_z, the axial component of the wave vector, and m, the angular momentum ($m = 0, 1, 2, \ldots$). For a given mode, the radial and angular components of the electric and magnetic fields can be calculated from the corresponding z (axial) components [35]. For a given wave vector k_z and angular momentum m, the axial field components in a layer of index n have the general form

$$\mathrm{F}(z, r, \phi) = [AJ_m(k_T r) + BY(k_T r)] \cdot \left(C_1 e^{im\phi} + C_2 e^{-im\phi}\right)$$

where F stands for either E_z or H_z; J_m and Y_m are Bessel functions of the first and second kind, respectively; and k_T is a transverse wave vector $k_T = \sqrt{(n\omega/c)^2 - k_z^2}$.

The modes of the coaxial omniguide are calculated with two different approaches. The first is a semianalytic approach based on the transfer matrix method [13]. Starting from Maxwell's equations, the z components of the electric and magnetic fields in each layer can be written in the general form given by Eq. 1. For given k_z, ω , and m, the only variables that determine the E_z and H_z fields are the four coefficients in front

of the Bessel functions (two for E_z and two for H_z). The boundary conditions at the interfaces between adjacent layers can be written in the form of a matrix equation

$$\begin{pmatrix} A \\ B \\ A' \\ B' \end{pmatrix}_{j+1} = \mathbf{M} \begin{pmatrix} A \\ B \\ A' \\ B' \end{pmatrix}_{j}$$

where $\begin{pmatrix} A \\ B \\ A' \\ B' \end{pmatrix}_{j}$ are the coefficients that determine the electric and magnetic fields in the jth layer, and $\mathbf{M}$ is a 4-by-4 transfer matrix that depends on k_z, ω , m, the geometry of the layers, and their indices of refraction. After calculating the electromagnetic fields for a given point (k_z, ω), we find the resonant modes by examining the fractional E-field power confinement in the coaxial waveguiding region; that is

$$\int_{r_i<r<r_o} d\mathbf{r}\, \epsilon(\mathbf{r})\, |E(\mathbf{r})|^2 \Big/ \int_{\text{all layers}} d\mathbf{r}\, \epsilon(\mathbf{r})\, |E(\mathbf{r})|^2$$

The second approach involves a numerical solution of Maxwell's equations in the frequency domain with the use of the conjugate gradient method within the supercell approximation [36]. Supercells of size ($30a$ by $30a$ by $0.1a$) were used, leading to a basis set of about 230,000 plane waves. Eigenvalues were considered converged when the residue was less than 10^{-6}. The results of both approaches were found to agree to better than 0.1%.

3.4 Modes of Coaxial Omniguide A

In the projected band structure for coaxial omniguide A (Fig. 3-2(c)), the red and yellow bands represent guided modes localized within the region defined by the inner and outer coaxial radii of the waveguide. The dashed lines represent modes with less than 20% localization within the coaxial region. There is close correspondence between the modes within the omnidirectional reflectivity range labeled $m = 1$ to $m = 6$ and those of the coaxial cable labeled TE_{11} to TE_{61}. The $m = 0$ mode appears to correspond to the TEM mode. Of course, for a coaxial omniguide with a limited number of outer shells, these modes can only exist as resonances. Nevertheless, even with only 2.5 bilayers, we find that they can be extremely well localized resonances, and the leakage rate decreases exponentially with the number of shells. The differences between the modes of a coaxial metal waveguide in Fig. 3-2(a) and those of coaxial omniguide A in Fig. 3-2(c) come from replacing the metal confining mirror with omnidirectional dielectric mirrors. The differences can be accounted for with a simple model based on the phase shift upon reflection off the mirror [8]. The main effect of the frequency-dependent phase shift of the dielectric mirror is that the dispersion relations of the guided modes are drawn towards the middle of the band gap when compared to their metallic counterparts.

The strong localization of the coaxial omniguide modes is shown in Fig. 3-3. Here, we plot the power density in the electric field for the four lowest frequency modes at $k_z = 0.19\,(2\pi/a)$. As the color bar indicates, power increases in going from black to dark red, to red, to orange, to yellow. The blue circles identify the boundaries between the various dielectric shells and are included as a guide to the eye. In all cases, the power is confined primarily within the coaxial region. This is particularly true for the $m = 0$ mode, which is also cylindrically symmetric, just like the TEM mode. Although it is well known that a waveguide consisting only of dielectric material cannot support a true TEM mode [37], we find that the $m = 0$ mode (which is a

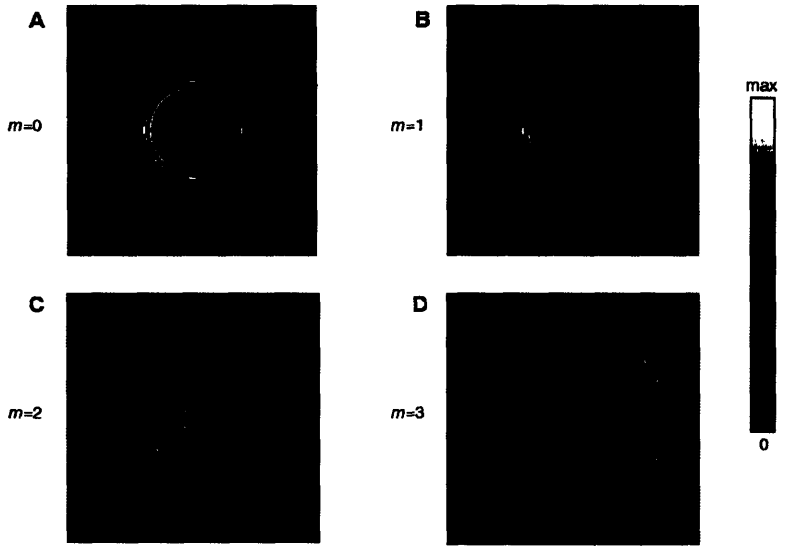

Figure 3-3: Power density in the electric field for guided modes at $k_z = 0.19\,(2\pi/a)$ in Fig. 3-2(c). Parts (a) through (d) correspond to guided modes with angular momenta $m = 0$ to $m = 3$, respectively. The color bar indicates that power increases in going from black to dark red, to red, to orange, to yellow. The blue circles identify the boundaries between the various dielectric shells and are included as a guide to the eye. Most of the power is confined to the coaxial region of the waveguide. The cylindrical symmetry and radial dependence of the $m = 0$ mode are consistent with those of a TEM mode. The small fluctuations in density away from perfect cylindrical symmetry in (A) are a consequence of the discrete square grid used in the computations.

pure TM mode) possesses several of the characteristics of the TEM mode. First, as mentioned above, it has zero angular momentum and hence a radially symmetric electric field distribution. Second, the electric and magnetic fields within the coaxial waveguiding region (where over 65% of the power is concentrated) are nearly identical to those of the metallic coaxial cable; for example, the predominant components are E_r and H_ϕ and they vary as $1/r$. Finally, at the point where the $m = 0$ dispersion curve (yellow line) crosses the light line, there is an exact correspondence between the electromagnetic fields of the coaxial omniguide and the metallic coaxial cable, inside the coaxial region. Moreover, the derivative of the group velocity is exactly zero near this point, leading to nearly dispersionless propagation in its vicinity.

3.5 Single-Mode Behavior in Coaxial Omniguide B

The characteristics described above are certainly the attributes one would hope to achieve in order to overcome problems with polarization-rotation and pulse broadening. But what about single-mode behavior? The bands shown in Fig. 3-2(c) are clearly multimode; that is, for a given frequency there are two or more guided modes that can be excited. To design a coaxial omniguide that can support single-mode behavior, we need only readjust our structural parameters. It is easier to keep the parameters of the bilayers fixed, so that the omnidirectional reflectivity frequency range does not change. This leaves only those parameters that are common to both the coaxial omniguide and the metallic coaxial cable: the inner and outer radii of the coaxial waveguiding region. Single-mode operation for the TEM-like mode will only be possible if all other modes are moved up in frequency so that the lowest nonzero angular mode has its cutoff frequency inside the bandgap. To do this, we have to decrease the inner radius of the coaxial waveguiding region. At the same time, the thickness of the bilayers, a, should remain constant, which means that we can no longer accommodate three bilayers in the inner part of the waveguide. Actually, the inner radius has to be decreased so much that we are forced to discard the periodic structure in the inner region and to replace it with a single dielectric rod. Loss of the inner-core mirror structure is not crucial, however. What is important is to add a thin rod of dielectric in the core in order to avoid the $1/r$ divergence of the field at the origin and to use a dielectric of high enough contrast to localize the TEM-like mode in the coaxial region. Testing different values for the inner and outer radii of the waveguiding region, we have found a configuration that has the desired properties. This new embodiment, coaxial omniguide B, is shown in Fig. 3-1(c). The central dielectric rod has an index of refraction $n_1 = 4.6$ and a radius $r_i = 0.40a$. The coaxial waveguiding region has an outer radius $r_o = 1.40a$, and the parameters of the outer bilayers are the same as those used for configuration A. In configuration B, there are

two frequency ranges where the waveguide can operate in a single-mode fashion. We plot the dispersion curves for the modes supported by coaxial omniguide B in Fig. 3-4. The yellow dots indicate more than 50% confinement of the electric field power, whereas the red dots represent confinement between 20 and 50%. (The dashed lines indicate confinement that is less than 20%.) The two white boxes identify the frequency ranges where the $m = 0$ band is single-mode. A comparison of Fig. 3-2(c) and Fig. 3-4 reveals that the cutoff frequency of the $m = 1$ band has shifted significantly upward, whereas the $m = 0$ band remains relatively unchanged. The flatness of the $m = 1$ band enables the TEM-like band to be single-mode both above it and below it in frequency. The exact values of the parameters were chosen so that, in the middle of the higher frequency single-mode window [at $\omega = 0.205\,(2\pi c/a)$], the mode is also dispersionless. The actual frequency bandwidth available for dispersionless transmission is determined from the dispersion slope which would be around $100\,\mathrm{ps/nm^2/km}$ at a wavelength of $1.55\,\mu\mathrm{m}$ [38]. This means, for example, that the dispersion remains below a level of 4 ps/nm/km in a frequency bandwidth of about 100 GHz, which could support a single 40 Gb/s channel. The flatness of the $m = 1$ band is due to a repulsion between this mode and the higher-frequency $m = 1$ mode. This is explained in more detail in Chapter 4, where it is shown that this mode repulsion can also lead to negative group velocity modes.

Figure 3-5 shows the distribution of the electric field components for the $m = 0$ mode of coaxial omniguide B at $k_z = 0.2\,(2\pi/a)$ and $\omega = 0.203\,(2\pi c/a)$. Because the (k_z, ω) point is very close to the light line, the electric field in the waveguiding region is almost completely transverse to the direction of propagation. (The z component of the magnetic field will always be zero because this is a pure TM mode.) The field distribution clearly reveals a high confinement of the mode in the waveguiding region, as desired. Moreover, these values of E_x and E_y lead to a net field distribution that is completely radially symmetric, consistent with an angular component that is exactly

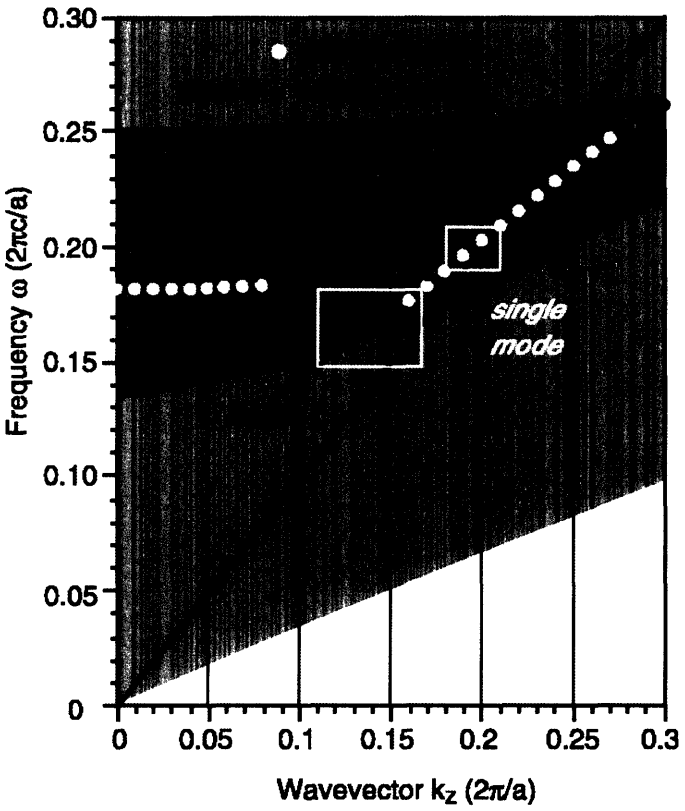

Figure 3-4: Projected band structure for coaxial omniguide B. The central dielectric rod has an index of refraction $n_1 = 4.6$ and a radius $r_i = 0.40a$. The coaxial waveguiding region has an outer radius $r_o = 1.40a$, and the parameters of the outer bilayers are the same as those used for configuration A. The yellow dots represent confinement of the electric field power of more than 50%; the red dots represent confinement between 20 and 50%; and the dashed lines represent confinement less than 20%. The two white boxes identify the frequency ranges where the $m = 0$ band exhibits single-mode behavior.

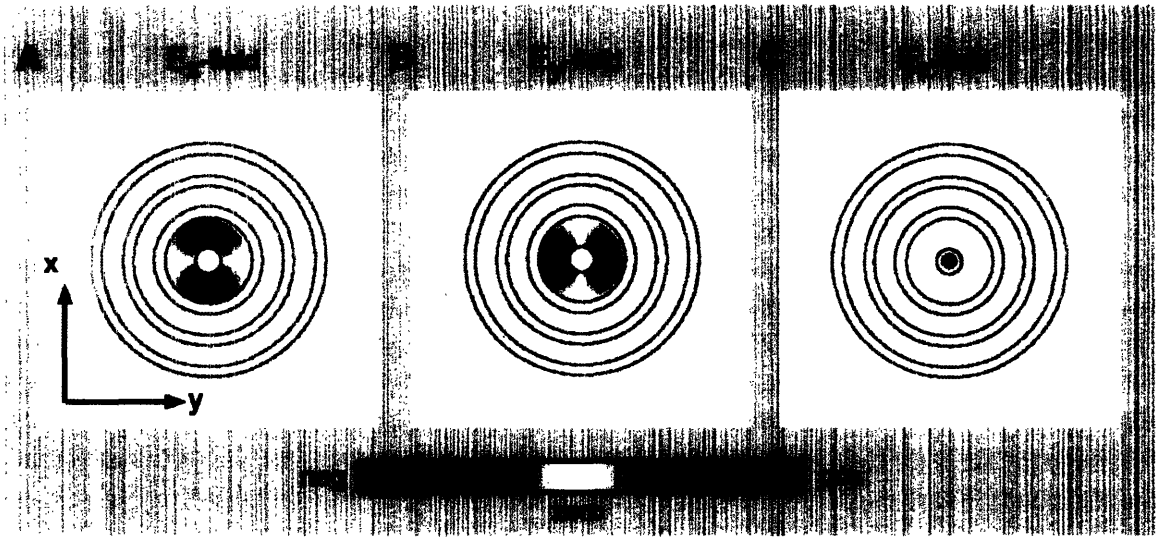

Figure 3-5: Electric field for the mode at frequency $0.203\,(2\pi c/a)$ and $k_z = 0.2\,(2\pi/a)$ in Fig. 3-4. Parts (a) through (c) are the electric field components along the x, y, and z directions, respectively. The color bar indicates that large positive and negative values are shown as dark red and dark blue regions, respectively, whereas white areas represent regions of zero values of the electric field, and light-colored areas represent regions of low values of the electric field. The field distribution clearly reveals a high confinement of the mode in the coaxial waveguiding region, and in this region it is nearly completely transverse to the direction of propagation (less than 10^{-3} of the intensity is along z), as desired.

zero. All the features mentioned above attest to the close correspondence between the $m = 0$ mode and a pure TEM mode.

There are several additional issues associated with the coaxial omniguide. The first is a practical issue involving the coupling of light into the coaxial omniguide. One possible method for coupling would be to begin with an omniguide with a very thin core that increases gradually to match the core of the coaxial configuration. Because the electromagnetic field of a laser source can have a TEM_{00} mode, this should lead to efficient coupling into the TEM-like mode of the coaxial omniguide. The second issue concerns the ability to transmit information across a broad band of frequencies with the coaxial omniguide. This is determined primarily by the width of the omnidirectional reflectivity range. Another issue is that the multitude of ad-

justable parameters in the structure of a coaxial omniguide (the index of refraction and thickness of each layer, the thickness of a bilayer, the waveguiding region inner and outer radii, the central rod index of refraction, and so on) allows for great flexibility in tuning the waveguide for optimal desired performance (confinement in the waveguiding region, width of single-mode window, frequency of zero dispersion, group velocity, and so on). A further important issue is that radial confinement of the light is a consequence of onidirectional reflection and not of total internal reflection. This means that the coaxial omniguide can be used to transmit light around much sharper corners than is possible with the optical fiber. Finally, the radial decay of the electromagnetic field in the coaxial omniguide is much faster than in the case of the optical fiber (with only 10 bilayers, one gets a decrease of electric field intensity of about six orders of magnitude). This means that, for guided light of the same wavelength, the outer diameter of the coaxial omniguide can be much smaller than the diameter of the cladding layer of the optical fiber without leading to cross-talk complications in waveguide bundles. These enabling characteristics of a substantially smaller waveguide bending radius and smaller spacing of adjacent waveguides lead to the possibility of substantial miniaturization of future integrated optical devices and transmission lines.

3.6 Summary

We presented an all-dielectric coaxial waveguide that combines some of the best properties of the coaxial metallic waveguide and all-dielectric index-guiding fibers. It consists of a coaxial waveguiding region with a low index of refraction, bounded by two cylindrical, dielectric, multilayer, omnidirectional reflecting mirrors. The waveguide can be designed to support a single mode whose properties are very similar to the unique transverse electromagnetic mode of a traditional metallic coaxial cable. The

new mode has radial symmetry and a point of zero dispersion. Moreover, because the light is confined by an omnidirection band gap and not by total internal reflection, the waveguide can guide light around sharp corners.

Chapter 4

Anomalous Dispersion Relations by Symmetry Breaking in Axially Uniform Waveguides[1]

4.1 Introduction

Axially uniform (constant cross-section) waveguides have been studied extensively for numerous applications, ranging from optical communications and integrated optics to microwave technology. Lateral confinement of light in waveguides is achieved either by total internal reflection (TIR) as in optical fibers [30], or by the use of a reflective cladding as in metallic waveguides [27], Bragg fibers [13, 25, 8], and photonic crystal fibers [40] (see Fig. 4-1). Typically, the guided modes of TIR waveguides have dispersion relations $\omega(k)$, frequency versus wavenumber, that are monotonic curves lying between the light lines associated with the lowest and highest indices of refraction in the structure. On the other hand, reflective-cladding waveguides

[1]This chapter is based in part on Ref. [39]: M. Ibanescu, S. G. Johnson, D. Roundy, C. Luo, Y. Fink, and J. D. Joannopoulos, "Anomalous dispersion relations by symmetry breaking in axially uniform waveguides," *Phys. Rev. Lett.* vol. 92, 063903, (2004).

can have dispersion relations that start from the $k = 0$ axis, as shown in Fig. 4-1(a). Ordinarily, these modes start with zero group velocity and have monotonically increasing dispersion relations as well.

In this chapter, we show by analytical and numerical methods that reflective-cladding waveguides of arbitrary cross-sectional symmetry can be made to support modes with anomalous dispersion relations, Fig. 4-1(b–d), that result from strong repulsion between a pair of modes in the vicinity of $k = 0$. When the axial wave vector is exactly zero, the two modes have different TE/TM symmetry and thus can be brought arbitrarily close to an accidental frequency degeneracy. For nonzero k, the symmetry is broken causing the modes to repel. We discuss unusual and counter-intuitive consequences that include backward waves, a reversed Doppler shift, reversed Cherenkov radiation, atypical singularities in the density of states, and a longitudinal length-scale determined purely by the transverse waveguide profile. The results are general because they have their origin in a reflection symmetry shared by all axially uniform waveguides.

4.2 Mode Symmetries in Axially Uniform Waveguides

Consider a lossless non-dispersive isotropic dielectric that is uniform in the z direction: $\epsilon(x, y, z) = \epsilon(x, y)$. The continuous translational symmetry implies that the axial wave vector k is a conserved quantity and that the magnetic field of a mode has the form $\mathbf{H}_k(x, y)\, e^{i(kz-\omega t)}$. The dispersion relation $\omega(k)$ and the field profile $\mathbf{H}_k(x, y)$ are obtained from the eigenvalue equation

$$\boldsymbol{\Theta}_k \mathbf{H}_k = \frac{\omega^2}{c^2} \mathbf{H}_k, \tag{4.1}$$

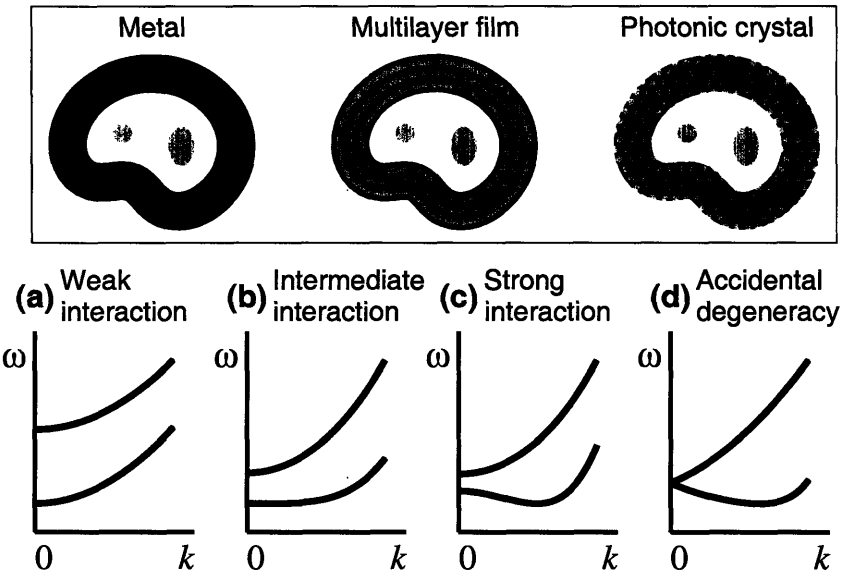

Figure 4-1: Top panel: Schematic drawings of the three types of reflective-cladding waveguides that employ metallic, multilayer-film, and photonic-crystal claddings. Bottom panel: Schematic band diagrams showing two neighboring modes as the relative frequency separation is decreased. At $k = 0$ one mode is TE polarized and the other TM polarized (the order is not important). (a) Weakly interacting modes. (b) A stronger interaction leads to a very flat lower band. (c) The repulsion between modes is strong enough to cause a backward wave region in the lower band. (d) Accidentally degenerate modes at $k = 0$ can have nonzero group velocity.

where

$$\Theta_k = (\nabla_t + ik\hat{\mathbf{z}}) \times \left(\frac{1}{\epsilon} (\nabla_t + ik\hat{\mathbf{z}}) \times \right) \tag{4.2}$$

and $\nabla_t = \frac{\partial}{\partial x}\hat{\mathbf{x}} + \frac{\partial}{\partial y}\hat{\mathbf{y}}$.

There are two spatial symmetries that all axially uniform waveguides possess: continuous translational symmetry in the z direction and reflection symmetry through the xy plane. In practice, typical waveguides might have additional symmetries such as rotations around the z axis or reflection into a vertical plane. We first consider waveguides with general non-symmetric cross-section and later deal with additional symmetries.

Let σ_h be the reflection in the transverse xy plane. The dielectric function $\epsilon(x, y, z)$ of a uniform waveguide is obviously symmetric under σ_h. However, the modes of the waveguide are not generally symmetric under σ_h because the axial wave vector k breaks this symmetry. A special case exists for $k = 0$, when the operator Θ_k still preserves the symmetry of ϵ. At $k = 0$, the modes have to be either even or odd with respect to σ_h. Even modes are said to have transverse electric (TE) polarization because their electric field is contained in the transverse plane; odd modes have transverse magnetic (TM) polarization. It is this symmetry that exists only at $k = 0$ that is responsible for effects presented below.

4.3 Mode Repulsion Caused by Symmetry Breaking

Consider now two neighboring TE and TM modes at $k = 0$, as shown in Fig. 4-1(a). The relative frequency separation between these two modes can be reduced by modifying the dielectric distribution $\epsilon(x, y)$. Because the orthogonality of these two modes at $k = 0$ is guaranteed by the TE/TM symmetry, it is generally possible to make the frequency separation arbitrarily small, as shown in Fig. 4-1(a–d), including the possibility of creating an accidental degeneracy.

Let us now examine the two modes and their dispersion relations at wave vectors k larger than 0. $\Theta_{k\neq 0}$ is no longer symmetric under reflection through the xy plane, and, since we are considering at this point only waveguides with general non-symmetric cross-section, Θ_k has no remaining symmetry at $k \neq 0$. The two modes no longer have pure TE or TM polarization, and now belong to the same irreducible representation. This leads to a repulsion between the two modes as seen in Fig. 4-1. The smaller the frequency separation at $k = 0$, the stronger the repulsion becomes.

Waveguides used in practice usually possess additional symmetries. For example, a circular waveguide has continuous rotational symmetry and is symmetric with respect to reflection across planes containing the z axis. In this case, in order to interact, the two modes must be chosen more carefully, such that at $k \neq 0$ the modes belong to the same irreducible representation. Thus, for the circular waveguide, the two modes must have the same angular quantum number. Concrete examples of strongly interacting modes will be given later.

We obtain quantitative results for the behavior of $\omega(k)$ in the vicinity of $k = 0$ by using perturbation theory for the eigenvalue equation for ω^2. We expand Θ_k in powers of k, and we treat the linear and quadratic terms as perturbations. The approach is similar to the $\mathbf{k} \cdot \mathbf{p}$ method used for electronic band structures. However, the derivation is complicated by the vectorial nature of the electromagnetic eigenvalue problem. Because of the constraint $\nabla \cdot \mathbf{H}(\mathbf{r}) = 0$, the physical modes at $k = 0$ do not form a complete basis in which to expand the modes at $k \neq 0$. The correct perturbation theory in k for electromagnetism was derived recently by Sipe [41]. Since for a non-degenerate mode at $k = 0$ the group velocity is zero, we use second-order perturbation theory to evaluate the second derivative of $\omega_n(k)$ at $k = 0$:

$$\left(\frac{\partial^2\omega_n}{\partial k^2}\right)_{k=0} = \frac{c^2}{\omega_n}\int\left(\left|\mathbf{E}_t^{(n)}\right|^2 + \frac{1}{\epsilon}\left|\mathbf{H}_t^{(n)}\right|^2\right)dxdy + \frac{c^2}{\omega_n}\sum_{\ell\neq n}\frac{\omega_\ell^2}{\omega_n^2-\omega_\ell^2}\left(\left|\int\hat{\mathbf{z}}\cdot\mathbf{E}_t^{(n)*}\times\mathbf{H}_t^{(\ell)}dxdy\right|^2 + \left|\int\hat{\mathbf{z}}\cdot\mathbf{E}_t^{(\ell)*}\times\mathbf{H}_t^{(n)}dxdy\right|^2\right). \tag{4.3}$$

Here, the index ℓ is summed over all modes of the waveguide, except for the nth mode. The integrals are over the entire cross-section. $\mathbf{E}_t^{(n)}$ stands for the transverse part of the normalized electric field for the nth mode at $k = 0$. The right hand side has two contributions: *(i)* the first term contains only the field of the nth mode itself and is always positive; *(ii)* the second term represents the interaction of the the mode of interest with the other modes of the waveguide. Contribution *(ii)* is negative for modes above the mode of interest ($\omega_\ell > \omega_n$) and positive for modes below the mode of interest ($\omega_\ell < \omega_n$). We interpret this term as a repulsion between modes, whose strength diverges as the frequency separation $\omega_n - \omega_\ell$ is taken to zero. Thus, although this term is relatively small for a typical waveguide, we can make it the dominant term by decreasing $\omega_n - \omega_\ell$. Also note that the interaction between two modes is nonzero only for modes of opposite TE/TM polarization.

4.4 Anomalous Dispersion Relations

The first unusual effect that results from the strong mode repulsion is the negative-slope region of the lower mode in Fig. 4-1(c–d). Modes for which $v_g = \partial\omega/\partial k$ and $v_\varphi = \omega/k$ have opposite signs are called "backward-wave" modes and were discovered in the context of dielectric-loaded circular metallic waveguides by Clarricoats and Waldron [42]. Based on empirical evidence, their existence has been associated with the near degeneracy of two modes of different polarization [43]. Below the minimum

frequency of the backward wave mode there are evanescent modes (not shown in Fig. 4-1) for which k^2 is not real. The existence of these complex modes has been studied in [44, 45, 46]. We believe that this work provides the necessary physical intuition for understanding the existence of backward waves and complex modes in waveguides with arbitrary cross-section.

We now discuss some remarkable effects based on backward waves. The wave momentum[2] $\hbar k$ of a photon associated with a such a wave is negative, *i.e.* it is oriented in the opposite direction to the propagation of the photon. Imagine that an atom placed inside the waveguide absorbs a backward wave photon via an atomic transition. The recoil momentum points towards the direction from which photon came, which means that negative radiation pressure is being exerted on the atom. Similarly the Doppler shift for light traveling in a backward wave is reversed. Finally, reversed Cherenkov radiation results from resonant radiation of a relativistic electron into a backward wave. While this effect has been discussed before in the context of periodically modulated structures [50, 51] and for negative index media [52], it is notable that it can be also obtained in a simple axially uniform waveguide.

Another peculiar feature resulting from strong mode repulsion is the possibility of having zero group velocity at a nonzero value of the wave vector, as in Fig. 4-1(c–d). Let $k_0 \neq 0$ be the wave vector where $v_g = 0$. The $(k_0, \omega(k_0))$ point of the dispersion relation is qualitatively different from all other points, and corresponds to a mode that does *not* transport energy but *does* have moving phase fronts. Moreover, the region of the dispersion relation between 0 and k_0 has all the characteristics of a band in the folded band structure of a medium that has periodicity $\Lambda = \pi/k_0$ in the axial direction — ironically, this longitudinal length-scale Λ is determined only by the transverse dielectric profile. To some degree, then, this uniform waveguide behaves as if it had a periodic corrugation in the axial direction. For potential applications,

[2]For a discussion on the differences between momentum, pseudomomentum and wave momentum of light see references [47], [48], and [49].

we note that the pitch Λ of this virtual corrugation can be modified dramatically by simply tuning the transverse profile of the waveguide. Also, the flat region of the dispersion relation around the $(k_0, \omega(k_0))$ point could be very useful in the field of waveguide nonlinear optics, where a small group velocity enhances nonlinear effects by a factor of c/v_g while the phase-matching criterion can still be satisfied because the wave vector is nonzero.

Another unusual feature is found in Fig. 4-1(d) for small values of k. If the two interacting modes are exactly degenerate, their group velocities remain constant as $k \to 0$. We can thus have, in an axially uniform waveguide, a propagating mode that has almost no axial phase variation. In terms of practical applications, a regular mode in the neighborhood of $k = 0$ has very small group velocity and thus becomes unusable because both the dispersion and the losses scale inversely with v_g and thus diverge as we approach $k = 0$. The modes in Fig. 4-1(d) do not have this problem because v_g is roughly a constant in the vicinity of $k = 0$.

Table 4.1: Possible Van Hove singularities in the density of states $D(\omega)$ corresponding to the lower mode in Fig. 4-1(a-d).

	$\left(\frac{\partial\omega}{\partial k}\right)_0$	$\left(\frac{\partial^2\omega}{\partial k^2}\right)_0$	$\left(\frac{\partial^3\omega}{\partial k^3}\right)_0$	$\left(\frac{\partial^4\omega}{\partial k^4}\right)_0$	$D(\omega)$
(a)	$= 0$	> 0			$(\omega - \omega_0)^{-1/2}$
(b)	$= 0$	$= 0$	$= 0$	$\neq 0$	$(\omega - \omega_0)^{-3/4}$
(c)	$= 0$	< 0			$(\omega_0 - \omega)^{-1/2}$
(d)	$\neq 0$				*const.*

The density of states (DOS) associated with the lowest of the two interacting modes varies dramatically between the four situations depicted in Fig. 4-1(a-d). The contribution of a mode to the DOS is inversely proportional to the group velocity $\partial\omega/\partial k$. More generally, at a singular point the type of Van Hove singularity [53] is determined by the first nonzero derivative of $\omega(k)$. A summary of possible behaviors is presented in Table 4.1, in which the four rows correspond to the four situations shown

in Fig. 4-1. Case (a) is the normal 1D divergence that is associated with the cut-off of a typical mode. In case (b) the mode repulsion is chosen to exactly cancel the second derivative of $\omega(k)$. Also, the third derivative is zero by time-reversal symmetry, which means the the first nonzero derivative is $\partial^4\omega/\partial k^4$. This extremely flattened dispersion relation leads to a very strong divergence of the DOS, which could be useful in the design of low-threshold lasers. Also, it would modify the radiative behavior of atoms inside the waveguide [54]. Of course, the cancellation of the second derivative cannot be achieved exactly in experiment. However, it is enough to have a very small second derivative in order to get a very large enhancement of the DOS. In case (c), the second derivative has a negative sign. Also, we have an additional singularity in the DOS coming from the minimum of $\omega(k)$ at a nonzero k (see Fig. 4-1(c)). Finally, case (d) corresponds to the accidental degeneracy at $k = 0$ of the two interacting modes. Because the group velocity is constant near $k = 0$, the contribution to the DOS coming from each of the modes is a Heaviside step function. The group velocities of the two modes are equal in magnitude, which means that the total contribution to the DOS is a constant. When the two modes are not exactly degenerate at $k = 0$ they each contribute a peak to the DOS. One can imagine making a waveguide in which the two modes can be tuned in and out of the degeneracy, thus turning on and off the two peaks in the DOS.

4.5 Waveguide Designs

As concrete examples of waveguides supporting modes with anomalous dispersion relations, we have performed numerical simulations for two all-dielectric waveguides as shown in Fig. 4-2. Both waveguide geometries should be experimentally realizable [28, 25, 40]. The actual parameters were chosen to exhibit Fig. 4-1(c) and (b) behavior.

The cylindrical Bragg waveguide in Fig. 4-2(a) confines light by means of a mul-

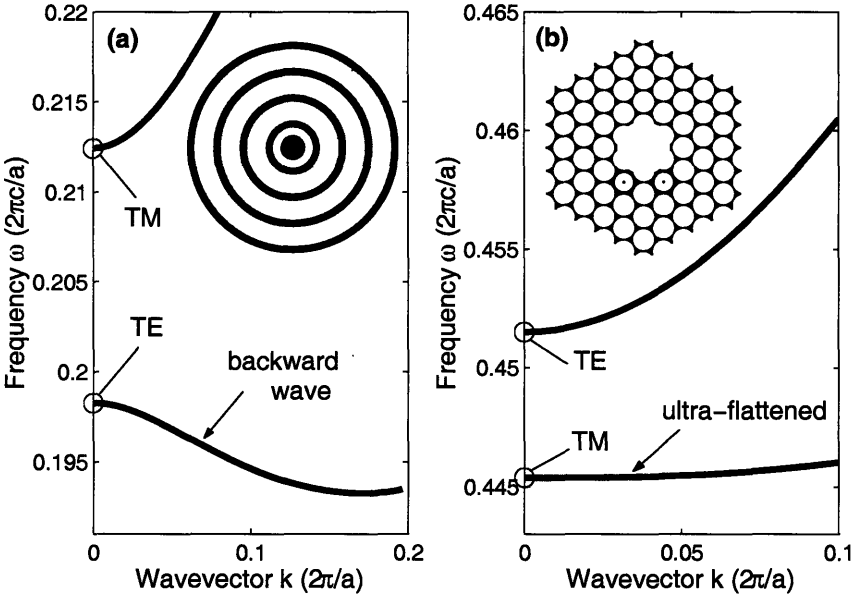

Figure 4-2: (a) Dispersion relations of two modes with angular momentum unity for the cylindrical waveguide in inset. The dark regions have an index of refraction 4.6 (*e.g.* Te), while the light gray regions have 1.4 (*e.g.* polymer). Starting from the center, the rod has a radius $0.45a$, the first ring has a thickness $0.32a$, the second one $0.23a$, and the following low/high index layers have thickness $0.75a/0.25a$, respectively. (b) Ultra-flattened dispersion relation in a photonic-crystal fiber with an index of refraction of 3.5 (*e.g.* semiconductor). The distance between two neighboring air holes is a and the radius of a normal hole is $0.46a$. The two dotted holes below the fiber core have a modified radius of $0.40a$.

tilayered periodic cladding [25]. We calculate its modes using a transfer matrix approach [13]. We focus on two strongly repelling modes that have angular quantum number unity. At $k = 0$ the lower mode is TE polarized, and the upper mode is TM polarized. The lower mode has a negative group velocity from $k = 0$ to $k_0 = 0.172\,(2\pi c/a)$, with a minimum group velocity $v_g = -0.05c$. It also has a point of zero group velocity at the nonzero wave vector k_0.

In the photonic-crystal fiber [40] of Fig. 4-2(b) light is confined by the complete band gap of a triangular lattice of holes. The modes of the structure were computed using a freely available frequency-domain solver [36]. We start with the bulk 2D photonic crystal and create a standard core by removing the seven central unit cells [40]. The resulting hollow waveguide supports modes that are similar to those of a hollow metal cylinder. We choose the pair of modes that are analogous to the degenerate pair TE_{01} and TM_{11} of the metal waveguide. Here, they are not exactly degenerate but have a relatively small frequency separation, which is favorable for a strong mode interaction. However, these modes do not interact because they transform differently under a reflection symmetry across a plane containing the waveguide axis. To allow the modes to interact we break the C_{6v} symmetry of the waveguide by decreasing the radius of two holes below the waveguide core. Thus, we obtain the cross-section and dispersion relations of Fig. 4-2(b). Although backward waves can be obtained here too, we instead choose a value for the radius of the two modified holes such that the lower mode has an extremely flat dispersion relation.

By using higher-order modes, waveguides with smaller index of refraction contrast can also be made to have anomalous dispersion relations. Because the typical relative frequency separation for these modes is smaller, they require a smaller perturbation in order to be made nearly degenerate. Thus, the high-index component of the waveguide could be made of chalcogenide glasses [28] with an index of up to 2.8. Finally, note that even though the modes in Fig. 4-2 lie above the light line, if the repulsion is

strong enough the anomalous nature of the modes can extend below the light line, leading to backward wave modes that are index guided.

4.6 Summary

We have shown that modes of axially uniform waveguides of arbitrary cross-section can be made to have anomalous dispersion relations resulting from strong repulsion between two modes. When the axial wave vector k is 0, the two modes have different TE/TM symmetry and thus can be brought arbitrarily close to an accidental frequency degeneracy. For nonzero k, the symmetry is broken causing the modes to repel. The strength of the repulsion diverges as the relative frequency cutoff separation of the modes is decreased towards zero, and this can lead to unusual features such as extremely flattened dispersion relations, backward waves, zero group velocity for nonzero k, atypical divergence of the density of states, and nonzero group velocity at $k = 0$. Although we only dealt here with the band structure of axially uniform waveguides, similar effects should be attainable in more complex systems, such as 2D and 3D photonic crystals.

Chapter 5

Phase Conjugation of Light Using a Negative Group Velocity Mode of an Axially-Uniform Waveguide

5.1 Introduction

In this chapter we show how the anomalous dispersion relations discussed in Chapter 3 can be combined with tunable waveguides to allow for novel approaches to the phase conjugation and the time delay of light pulses. By inducing an adiabatic spatially-uniform change to the waveguide properties (*e.g.* refractive index) the group velocity of the guided light can be modified while maintaining the axial wave vector as a conserved quantity. Combining this with the anomalous dispersion relations of the previous chapter, it is possible to *(i)* introduce arbitrarily large time delays by making the group velocity zero, or to *(ii)* achieve phase conjugation and time reversal of light pulses by changing the sign of the group velocity. Phase conjugation is traditionally achieved through nonlinear processes such as four-wave-mixing and requires two counter-propagating pump beams at a frequency determined by the signal

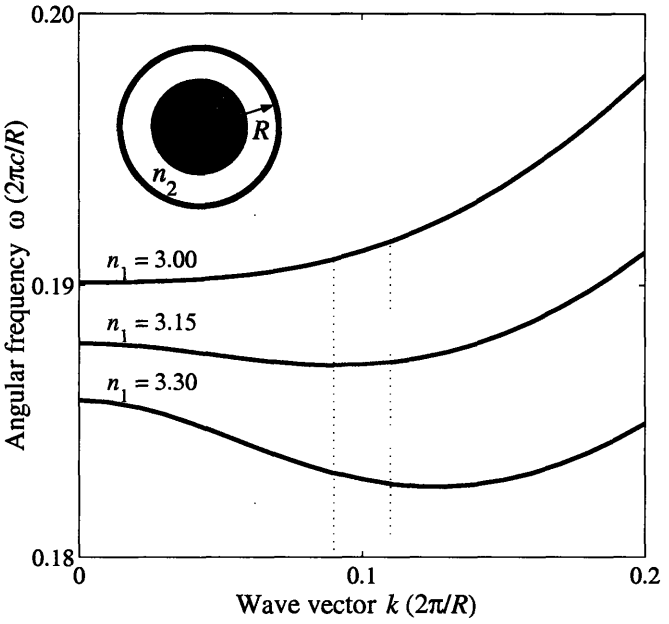

Figure 5-1: Dispersion relations of the tunable waveguide for three values of the index of refraction of the central rod, $n_1 = 3.00$, 3.15, and 3.30. For wave vectors around $0.1\,(2\pi/R)$ the group velocity can be changed from positive to zero and even negative values.

frequency [55]. Time delay lines are typically implemented with fiber Bragg gratings and rely on the reduced group velocity found in a narrow frequency range around a photonic band gap. Recently an interesting new approach has been presented that in which both time delay and time reversal of optical pulses can be obtained in a tunable two-dimensional photonic crystal coupled-cavity waveguide [56, 57]. The basis for that work is that the dispersion relation of the waveguide mode can be tuned to have positive, zero, or negative group velocity at a given wave vector. These dramatic changes in the dispersion relation of the mode are made possible in part by the band folding associated with a periodic structure [3]. Here, we present a simpler, more fundamental implementation of both time delay and time reversal of light in an *axially-uniform* waveguide that supports a mode with truly negative group velocity. The fact that our approach could be implemented in an in-fiber device is advantageous because relatively long devices are needed to accomodate entire optical pulses.

5.2 Phase Conjugation

The key element to our proposed scheme is a tunable waveguide in which a pulse is made to propagate at a group velocity that can be tuned from positive to zero or negative values, as shown in Fig. 5-1. A device for time reversal (phase conjugation) of light would operate with the top and bottom curves, which have group velocities of opposite sign. A pulse enters the unperturbed waveguide and propagates down its length according to the dispersion relation corresponding to $n_1 = 3.00$ (top curve) in Fig. 5-1. After the entire pulse has entered the waveguide we tune the dispersion relation by slowly introducing a a spatially-uniform perturbation to the waveguide such that the index of refraction of the core changes to $n_1' = 3.30$. Because the perturbation is spatially-uniform the longitudinal wavevector k is still a conserved quantity. If we imagine decomposing the pulse of light into spectral components, we see that the low frequency components of the incoming pulse correspond to the low wave vectors (positive group velocity). After the waveguide has been tuned to $n_1' = 3.30$ the wave vectors are conserved, but now the lowest wave vectors correspond to the highest frequncy components of the outgoing pulse (negative group velocity). The outgoing pulse travels back towards the input has been phase-conjugated because the frequency spectrum has been flipped (shown schematically in Fig. 5-2).

5.3 Time delay

5.4 Summary

We use a negative group velocity mode of a tunable axially-uniform waveguide to obtain time reversal of an optical pulse. The frequency spectrum of the pulse is reversed when a spatially-uniform perturbation is applied adiabatically to the waveguide such that the group velocity of the operating mode changes sign. We also present simula-

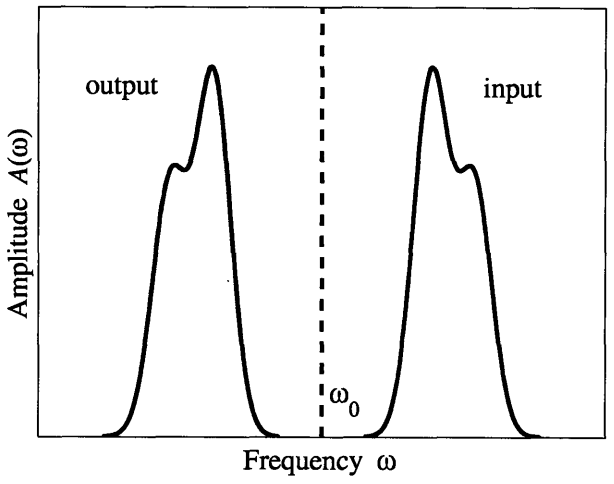

Figure 5-2: The frequency spectrum of a pulse is flipped as a result of phase conjugation.

tion results for a dispersion compensation scheme where phase conjugation is applied at the middle of a transmission line.

Chapter 6

Microcavity Confinement Based on Anomalous Zero Group-Velocity Waveguide Mode[1]

6.1 Introduction

Optical microcavities with small modal volumes and large quality factors are required in a wide range of applications and studies, such as low-threshold lasers, small optical filters, nonlinear optics and, strong-coupling cavity quantum electrodynamics [59, 60, 61, 62, 63, 64]. Cavities with a modal volume V on the order of λ^3 tend to have quality factors Q that are limited by radiation loss. Several mechanisms have been used to improve Q without sacrificing the small modal volume: the use of a complete photonic band gap in a 3D photonic crystal [4]; perfect mode-matching in a cylindrical Bragg resonator [65]; Fourier-space analysis of the field distribution in a photonic crystal slab cavity [66, 67]; and multipole-cancellation in a photonic crystal

[1]This chapter is based in part on Ref. [58]: M. Ibanescu, S. G. Johnson, D. Roundy, Y. Fink, J. D. Joannopoulos, "Microcavity confinement based on an anomalous zero group-velocity waveguide mode ," *Opt. Lett.* vol. 30, 552–554, (2005).

slab cavity [68]. Here, we introduce a fundamentally different mechanism based on small group-velocity propagation of light in a short piece of a uniform waveguide. The small group velocity v_g results in a large Q in two ways: *(i)* it increases the round-trip travel time $2L/v_g$ inside the cavity, and *(ii)* it increases the impedance mismatch between the cavity and the outside space, thus decreasing the fraction of power lost at each reflection from the boundaries (even though the structure includes no conventional high-quality mirrors in the axial direction). A critical requirement is that this zero group velocity be associated with a nonzero wave vector so that the Fabry-Perot resonance condition can be met.

6.2 Zero Group Velocity at a Nonzero Longitudinal Wave Vector

The design of the cavity is based on the possibility of *uniform* waveguides to support modes with zero group velocity at a nonzero longitudinal wave vector. It has been shown recently [39] that such modes can be created in waveguides of arbitrary cross section, provided that the waveguides have a reflective cladding, such as a metal layer, a dielectric mirror, or a 2D photonic crystal cladding. To demonstrate the novel high-Q mechanism, we first consider a simple cavity based on an idealized dielectric-loaded metal waveguide. Later, we show how the same mechanism can be exploited in a realistic structure by designing an all-dielectric high-Q cavity.

Let us first consider the dielectric-loaded metal waveguide whose cross section is shown as an inset in Fig. 6-1. Inside a metal cylinder of inner radius a, we have a dielectric rod of radius $0.65a$ and index of refraction $n_1 = 3.50$ surrounded by a region with a low index of refraction $n_0 = 1$. Dispersion relations, angular frequency ω versus longitudinal wave vector k, are shown for the lowest two guided modes with angular momentum unity: HE_{11} and EH_{11}. A strong repulsion between the two

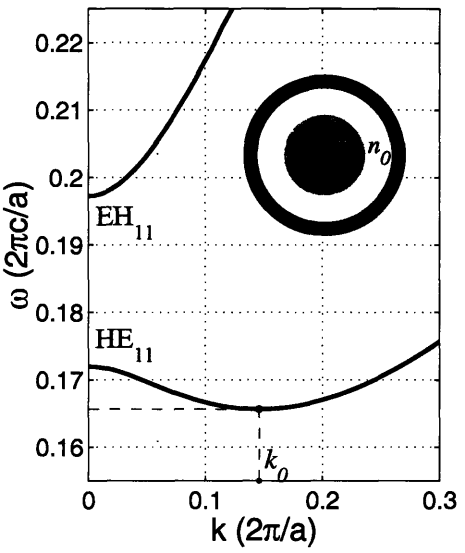

Figure 6-1: Band structure of the axially-uniform dielectric-loaded metal waveguide (inset) showing the lowest two modes. The lower mode is anomalous with a non-trivial point of zero group velocity at $k_0 = 0.146\,(2\pi/a)$, $\omega_0 = 0.1656\,(2\pi c/a)$.

modes is visible for wave vectors $k > 0$, due to the removal of a TE/TM symmetry that exists only at $k = 0$ [39]. As a result, the lower mode acquires an anomalous dispersion relation that includes a region of backward-wave propagation [42] for k less than $k_0 = 0.146\,(2\pi/a)$, as well as a point of *zero* group velocity at wave vector k_0 and frequency $\omega_0 = 0.1656\,(2\pi c/a)$. This special point of the dispersion relation introduces a longitudinal length scale $\Lambda = 2\pi/k_0 = 6.85a$ in a waveguide that is otherwise uniform. Now, imagine an optical cavity that is simply a piece of length L of the above waveguide, surrounded by vacuum, as shown in Fig. 6-2(a). The resonant modes of the cavity obey the condition that the round-trip accumulated phase $2kL + 2\Delta\phi$ is a multiple of 2π, where $\Delta\phi$ is the phase shift associated with reflection from the boundary and is roughly independent of L. For lengths L separated by $\Lambda/2 = \pi/k_0$, the resonance condition is met for wave vectors close to k_0 and therefore the Q of the resonant mode should be enhanced by the low group velocity. Thus, we expect $Q(L)$ to have a periodic enhancement, with periodicity $\Lambda/2$.

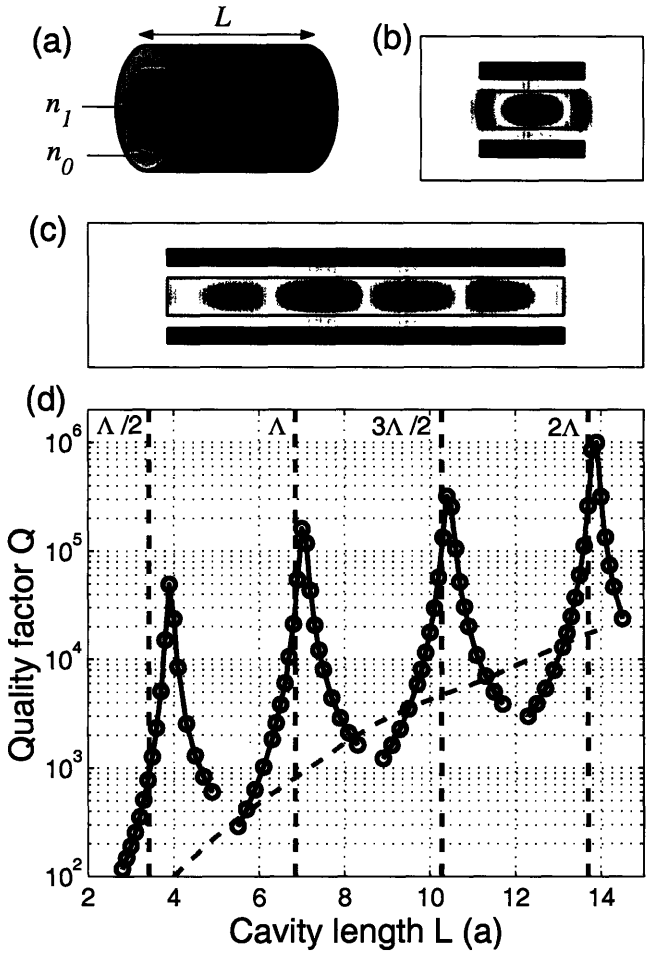

Figure 6-2: (a) A piece of length L of the waveguide in Fig. 6-1 can form a high-Q cavity. (b) Resonant mode in cavity of length $L = 3.9a$. In an axial cross section, we show the electric field component perpendicular to the plane, with the red and blue regions corresponding to positive and negative values. The metal cladding is shown in black. Note that the FDTD computational cell is actually larger than the rectangular box shown here. (c) Resonant mode for $L = 13.9a$. (d) The quality factor Q is plotted as a function cavity length L. The red circles are the results of FDTD simulations, while the dashed vertical lines correspond to multiples of $\Lambda/2$. Also shown as a blue dashed line, is the $Q(L)$ curve for a cavity based on a modified waveguide that does not have $v_g = 0$ at $k \neq 0$.

6.3 New Mechanism for Confining Light

We analyze the resonant modes of the cavity via finite-difference time-domain (FDTD) simulations, using a resolution of 20 grid points per a and perfectly-matched absorbing boundary layers [69]. To speed up calculations, we discretize the structure over a cylindrical grid and impose an angular field dependence of the form $e^{i\varphi}$, thus selecting only modes with angular momentum unity and reducing a full 3D problem to a 2D simulation. We excite the resonant mode of interest with a Gaussian pulse and then monitor the radiative decay of the field. The frequencies and quality factors of resonant modes are extracted using a filter-diagonalization method that decomposes a time series into a sum of decaying sinusoids [70]. In Fig. 6-2(b) we show the high-Q resonant mode found in a cavity of length $L = 3.9a$. It has angular frequency $0.1711\,(2\pi c/a)$, quality factor $Q \simeq 49,000$ and modal volume $0.6\,(\lambda/n_1)^3$. Similarly, for $L = 13.9a$, Fig. 6-2(c) shows a mode with $\omega = 0.1622\,(2\pi c/a)$, $Q \simeq 1.0 \times 10^6$ and modal volume $1.4\,(\lambda/n_1)^3$. From the two field patterns, we can see that these two resonant modes are based on the same mode of the uniform waveguide, the main difference being the number of half-wavelengths that fit inside the cavity: one and four, respectively. Figure 6-2(d) shows on a semi-logarithmic scale how Q varies with the length of the cavity L. We plot the $Q(L)$ curve as four disconnected sections because the mode with the highest Q value changes from having one half-wavelength in the cavity to having two, three or four half-wavelengths. The immediate qualitative conclusion from Fig. 6-2(d) is that there is indeed a longitudinal length scale associated with the waveguide, this being reflected in the periodic behavior of $Q(L)$. Moreover, the cavity lengths for which $Q(L)$ peaks are separated almost exactly by $\Lambda/2$. Actually, the peak lengths themselves lie very close to the multiples of $\Lambda/2$ shown as dashed vertical lines in the figure, which is consistent with a reflection phase shift $\Delta\phi$ being close to π. As L becomes larger, the frequency of the resonant mode converges quadratically to ω_0, the frequency of zero group velocity in the uniform waveguide.

n_1	$k_0\,(2\pi/a)$	$L_4\,(a)$	$2k_0L_4$
3.50	0.146	13.9	8.08π
3.70	0.161	12.4	8.02π
3.90	0.172	11.6	7.98π

Table 6.1: Conservation of round-trip phase shift.

All of the above support our conclusion that the high-Q resonant mode has indeed its origin in the zero group velocity mode of the waveguide, and that the longitudinal length scale Λ of the waveguide is critical for determining the cavity lengths for which Q is a maximum. For comparison, the dashed blue curve in Fig. 6-2 is the same $Q(L)$ curve for a waveguide in which the radius of the central rod has been reduce to $0.40a$. This waveguide still has a flattened dispersion relation for the HE_{11} mode, but does not have a mode with $v_g = 0$ at $k \neq 0$, and thus its $Q(L)$ curve does not possess any periodicity.

To verify that the above results are general and not just a coincidence for a particular waveguide structure, we repeat the $Q(L)$ calculations for other values of the dielectric rod refraction index n_1, and the results are summarized in Table 6.1. For each value of n_1 we list the wave vector k_0 for which the waveguide mode has zero group velocity and the cavity length L_4 that corresponds to the fourth peak of the curve $Q(L)$. Our simple model based on the round-trip phase shift predicts that $2k_0L_4$ should be in the neighborhood of 8π. Indeed, we find that the fourth column of the table lists numbers close to the predicted value. Moreover, a change in k_0 of about 10% between $n_1 = 3.50$ and $n_1 = 3.90$ results in a change of only 1% for the phase shift $2k_0L_4$.

6.4 All-Dielectric High-Q Cavity

Having shown that zero group velocity modes can lead to high-Q resonances, we apply this novel mechanism to the design of an all-dielectric high-Q cavity. As shown

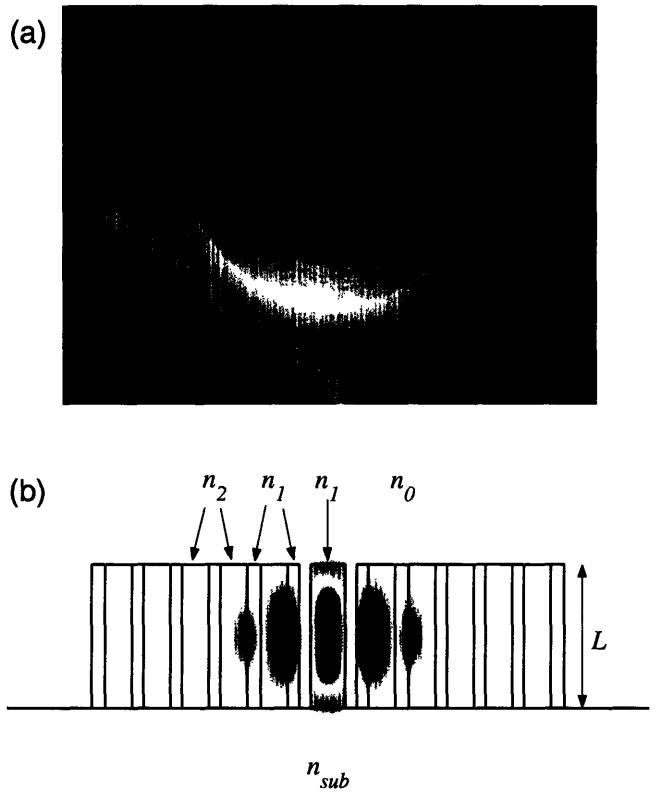

Figure 6-3: (a) A cylindrical all-dielectric cavity. (b) The axial cross section shows the cavity structure: on top of a substrate with refraction index n_{sub}, we have a central rod with index n_1 followed by a region with index n_0 and surrounded by a Bragg mirror that confines light to the core region. The electric field component perpendicular to the plane is shown in a color plot.

in [39], modes with zero group velocity at a nonzero wave vector can be found in dielectric waveguides such as cylindrical Bragg fibers and photonic crystal fibers. Here we choose the former waveguide type as an example, and design a cavity geometry, shown in Fig. 6-3, that should be manufacturable by lithographic methods. The core part is similar to the cavity presented before: a central rod with index $n_1 = 3.50$ (*e.g.* silicon) and radius $0.60a$, surrounded by a region with index of refraction $n_0 = 1$ up to a radius a. The rest of the structure is the Bragg mirror that confines light to the core region. The mirror is made of alternating layers: high index layers with index n_1 and thickness $d_1 = 0.40a$, and low index layers with $n_2 = 1.45$ (*e.g.* silica) and $d_2 = 0.95a$.

The cavity sits on a bulk substrate with index n_{sub}. We calculate the modes of a uniform waveguide having the same cross section parameters and we find a bandgap-guided mode with zero group velocity at $k_0 = 0.12\,(2\pi/a)$, $\omega_0 = 0.182\,(2\pi c/a)$. From the previous example we expect to create a high-Q resonant mode when the cavity length, height in this case, is around $\Lambda/2 = \pi/k_0$. Indeed, for $L = 4.8a$ and a symmetric structure with $n_{sub} = n_0 = 1$, we find a resonant mode with frequency $0.184\,(2\pi c/a)$, $Q = 17,000$ and modal volume $1.1\,(\lambda/n_1)^3$. In the core region, the field distribution shown in Fig. 6-3(b) is very similar to that obtained for the analogous metallic cavity. Also, the frequency of the resonant mode is close to ω_0. Thus, we conclude that this large Q value is also due to the special zero group velocity point of the dispersion relation. Analyzing the field pattern of the resonant mode we find that most of the power radiates in the longitudinal direction which would be desirable for butt-coupling to a fiber, for example. Taking a higher value for the substrate refraction index leads to a decrease in Q because the power leaks out more easily into a high refraction index region. For $n_{sub} = 1.30$ and $L = 5.00$ the quality factor is reduced by about 50% to $Q = 7,500$. Since this reduction factor is about the same for longer cavities, larger Q values could be obtained for cavities designed to fit higher-order resonant modes as in Fig. 6-2(d).

6.5 Summary

We propose and demonstrate a new mechanism for small-modal-volume high-Q cavities based on an anomalous uniform waveguide mode that has zero group velocity at a nonzero wave vector. In a short piece of a uniform waveguide having a specially designed cross section, light is confined longitudinally by small group velocity propagation and transversely by a reflective cladding. The quality factor Q is greatly enhanced by the small group velocity for a set of cavity lengths that are separated by

approximately π/k_0, where k_0 is the longitudinal wave vector for which the group velocity is zero. We demonstrated the mechanism in a simple metal cavity and showed that the same mechanism can be applied to all-dielectric cavities as well. It is our hope that, by itself or in combination with previously studied mechanisms, this new high-Q mechanism will allow for the design and fabrication of improved optical microcavities.

Chapter 7

Enhanced Photonic Band-Gap Confinement via Van Hove Saddle Point Singularities

7.1 Introduction

In this chapter, we move our attention to photonic band gaps of crystals with periodicity in two or more directions. We show that a saddle-point van Hove singularity in a band adjacent to a photonic crystal band gap can lead to photonic crystal structures that defy the conventional wisdom according to which the strongest band-gap confinement is found at frequencies near the midgap. The applications of these results could be quite wide as the confinement of light by photonic band gaps is at the base of a majority of photonic crystal devices and applications [1, 2, 4, 71, 72, 73]. For the simplest photonic crystal, a one-dimensional Bragg grating, the strongest confinement is found near the midgap frequency, and this intuitive result is often extended to higher-dimensional photonic crystal structures as well. However, in a recent article [74], Li *et al.* have reported numerical results showing a surprising fre-

quency dependence of the band-gap localization of a mode in a two-dimensional (2D) photonic crystal waveguide. The strongest localization was found not at the midgap frequency, but at frequencies much closer to the upper edge of the complete band gap. Here, we discover the origin of this effect as a consequence of the presence of a saddle point van Hove singularity in the dispersion relation of the photonic band immediately above the gap. Furthermore we argue that this effect is quite general, an intrinsic property of the *bulk* band structure, and could be used to design many other more effective photonic band-gap structures. In general, such interior saddle points in the band structures of 2D and 3D photonic crystals can be tuned to create photonic bands with very flat regions which, in turn, result in enhanced confinement at nearby band-gap frequencies.

To illustrate our results we use the example photonic crystal waveguide structure analyzed by Li *et al.* As shown in Fig. 7-1(a), a waveguide is created by removing a row of rods from a square lattice of dielectric rods in air. The lattice period is a and the rods have radius $0.18a$ and index of refraction 3.4. For the transverse magnetic polarization (magnetic field in the plane), the photonic crystal possesses a complete photonic band gap in the angular frequency range 0.302–0.443 $(2\pi c/a)$. Band-gap confinement results in a guided mode of the waveguide, whose field profile is shown schematically as a red line and whose dispersion relation is plotted as a black line in Fig. 7-1(b). If the surrounding photonic crystal cladding has only a finite number of layers some of the power in the waveguide mode will radiate outside and the mode becomes leaky [74, 75]. During numerical experiments on this waveguide mode, Li *et al.* observed a surprising frequency dependence of the loss coefficient. Instead of finding the lowest loss at a frequency close to the midgap frequency, they found that the radiation loss keeps decreasing as the frequency is increased almost to the upper limit of the complete photonic band gap. They also confirmed that this lower loss is consistent with a more tightly localized mode.

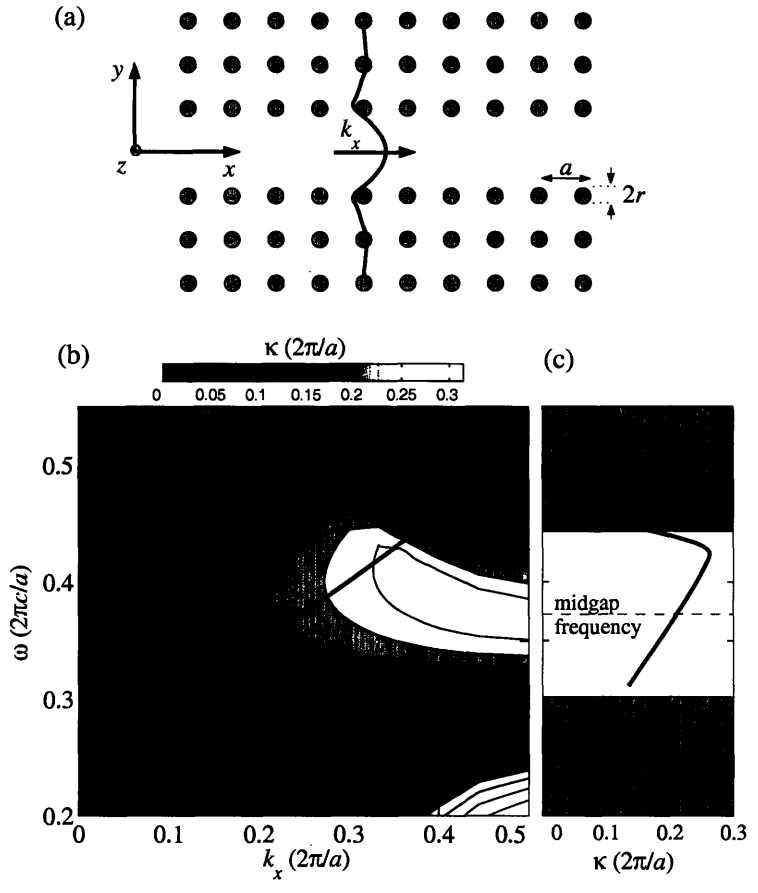

Figure 7-1: (a) A waveguide is formed by removing one row from a 2D square lattice of dielectric rods with refractive index 3.4 and radius $r = 0.18a$. (b) The dispersion relation of the waveguide mode (thick black line) is shown on top of a color contour plot of the confinement strength of the bulk photonic crystal $\kappa(\omega, k_x)$. The black regions include (ω, k_x) pairs for which propagating modes exist in the bulk crystal, while the colors from dark red to bright yellow, represent increasingly stronger confinement, as shown by the colorbar. (c) Confinement strength κ along the dispersion relation of the guided mode. The gray areas delimit the complete band gap range. The y-axis is the same as in part (b).

7.2 Evanescent Modes of the Bulk Photonic Crystal

To understand the localization of the waveguide mode in the transverse (y) direction, we investigate the properties of the evanescent bulk modes that make up the cladding tails of the waveguide mode. For a given frequency ω and longitudinal Bloch wave vector k_x, let $\{k_y^{(n)}\}$ be the infinite set of solutions for the transverse wave vector k_y of the bulk photonic crystal modes, with n being an integer index. (In vacuum, with the same boundary conditions, the solutions would by $k_y^{(n)} = \left[(\omega/c)^2 - (k_x + 2n\pi/a)^2\right]^{1/2}$). Band-gap confinement exists only at (ω, k_x) pairs for which all k_y solutions have a non-zero imaginary part and are therefore evanescent in the y-direction. For values of y far from the core of the waveguide the slowest-decaying mode dominates, which means that the strength of the band gap confinement is best described by the smallest imaginary part of k_y over all solutions [76]. Thus, we define the confinement strength to be $\kappa(\omega, k_x) = \min_n \left(\left| \mathrm{Im} \left[k_y^{(n)}(\omega, k_x) \right] \right| \right)$.

The complex-valued transverse wave vectors $k_y^{(n)}$ of the bulk crystal modes are calculated with CAMFR, a freely-available code that employs a frequency-domain eigenmode-expansion method [77]. From the set of $k_y^{(n)}$ values we extract the confinement strength κ and we present the results as a color contour plot in Fig. 7-1(b). The black regions correspond to no confinement since propagating states exist in the bulk crystal for those (ω, k_x) pairs. Red and yellow regions represent increasingly stronger confinement, as shown in the colorbar. Fig. 7-1(c) displays the strong asymmetry of the confinement strength $\kappa(\omega)$ along the dispersion relation of the guided mode. Instead of finding the strongest confinement at a frequency near the midgap, we see that κ increases throughout most of the complete band gap up to a frequency of $0.425\,(2\pi c/a)$, very close to the upper edge of the gap.

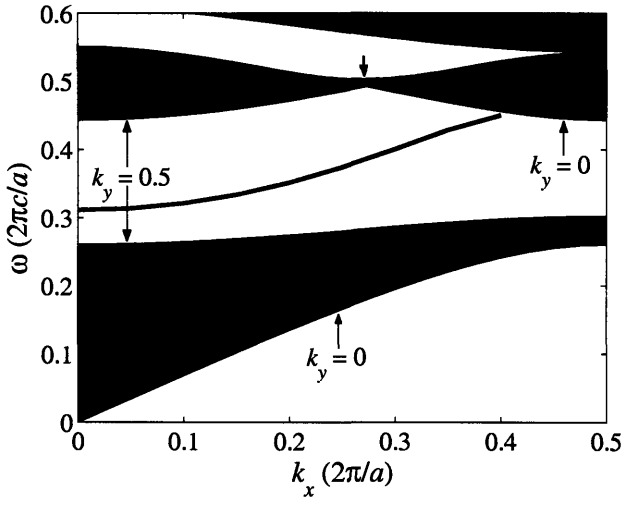

Figure 7-2: The projected TM band structure of the bulk crystal is shown by the blue areas and the black lines that represent $\omega(k_x)$ curves at constant k_y values ranging from 0 to 0.5 $(2\pi/a)$ in steps of 0.05 $(2\pi/a)$. Note that the second band of bulk crystal has a saddle point singularity that is indicated by a thick black arrow. Also shown is the dispersion relation of the fundamental waveguide mode (red curve).

7.3 Enhanced Confinement via Saddle Point

The key to this anomalous band-gap confinement can be found by looking at the bulk photonic crystal band structure which is shown in blue in Fig. 7-2. The lowest photonic bands $\omega(k_x, k_y)$ are plotted as a set of $\omega(k_x)$ curves at constant k_y values ranging from 0 to 0.5 $(2\pi/a)$ in steps of 0.05 $(2\pi/a)$. We note in particular the twisted shape of the second band, which is due to a saddle-point van Hove singularity located at $k_{x,s} = k_{y,s} = 0.269\,(2\pi/a)$, $\omega_s = 0.504\,(2\pi c/a)$ and marked in Fig. 7-2 by a thick arrow. Because of the square symmetry of the crystal, the saddle point is oriented with the maximum positive curvature in the ΓM ($k_x = k_y$) direction, and the maximum negative curvature in the perpendicular direction. As a result, the curvature in the x and y directions is very small (also see Fig. 7-4(d)). This, together with the requirement of zero group velocity of the bands at the Brillouin zone edge, translates into a very flat band $\omega(k_y)$ at $k_x = k_{x,s}$, the relative width of the band from one Brillouin zone edge to the other being just 2% of the central frequency.

The saddle-point singularity leads to a complex structure of the evanescent modes and to enhanced confinement strength at band-gap frequencies immediately above or below it. For the case of the waveguide mode considered here, it is the region below the saddle point that can be exploited. To show this, in Fig. 7-3(a–d) we plot the complex-valued $k_y^{(n)}$ solutions for the bulk as a function of frequency for four different values of the axial wave vector k_x: 0, 0.2, 0.3 and $0.5\,(2\pi/a)$. In each plot, the real and imaginary parts of $k_y^{(n)}$ are plotted side by side. In the frequency range of interest only the two lowest-order solutions, $n = 0$ and $n = -1$, have relatively small imaginary parts. We can safely ignore higher-order evanescent modes that are much more rapidly decaying and do not contribute to the overall confinement strength κ. For $k_x = 0$ (Fig. 7-3(a)), we locate a photonic band gap in the frequency range 0.26–$0.44\,(2\pi c/a)$. The gap is qualitatively similar to the gap of a one-dimensional photonic crystal: it is relatively symmetric, with the maximum confinement strength near the middle of the gap. Also the gap is bounded below and above (points A and B) by propagating solutions belonging to the same mode ($n = 0$). However, when we move to larger values of k_x we see dramatic changes in the nature of the band gap and in the nature of the photonic band just above the gap. Due to the presence of the saddle point, the second band changes slope from $k_x = 0$ to $k_x = 0.5$ and goes through an intermediate ultra-flat regime as seen for $k_x = 0.3$ (Fig. 7-3(c)). In this ultra-flat regime, the small curvature of $\omega(\mathrm{Re}[k_y])$ near the cutoff points B and C translates into an equally small curvature for $\omega(\mathrm{Im}[k_y])$ just below the cutoffs. As a result, the confinement map becomes very asymmetric. This can be clearly seen at $k_x = 0.3$, for example, where the confinement strength increases sharply as we move down in frequency from the cutoff at point C. To be more quantitative, we note that in the upper part of the gap the confinement strength reaches $\kappa = 0.20\,(2\pi/a)$ at a frequency that is only $0.017\,(2\pi c/a)$ below the gap edge C, while in the lower part of the gap, the same confinement strength is reached at a frequency $0.052\,(2\pi c/a)$ above

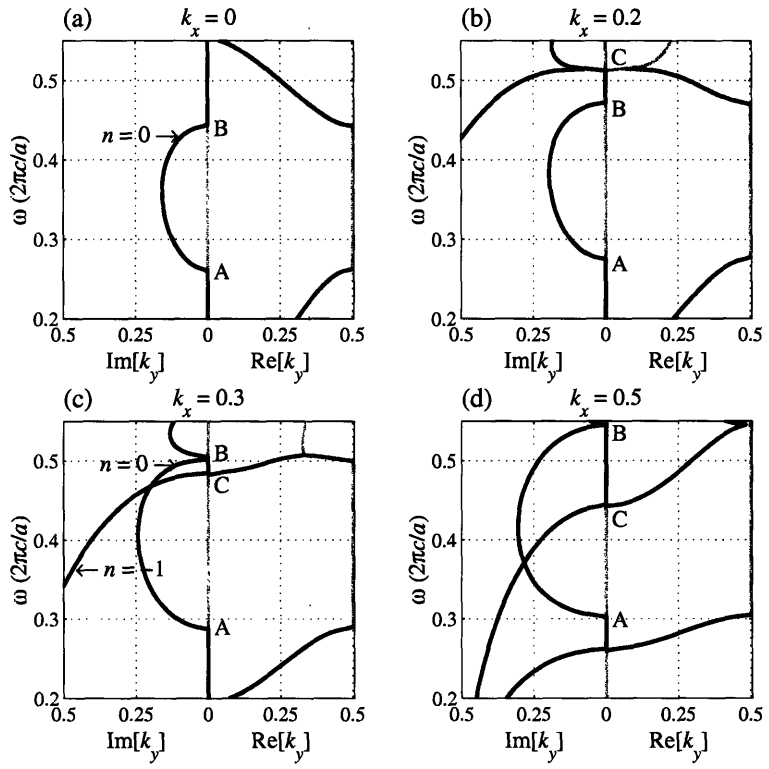

Figure 7-3: Dispersion relations $\omega(k_y^{(n)})$ at fixed k_x for propagating and evanescent modes in the bulk crystal. The axial wave vector k_x takes the values 0, 0.2, 0.3, and $0.5\,(2\pi/a)$ for parts (a) through (d). The imaginary part of $k_y^{(n)}$ is shown in red on the left side of each plot, while the real part is shown on the right, in blue for propagating modes and gray for evanescent and complex modes. In parts (a) and (c), the individual modes $k_y^{(n)}$ are labeled by the value of their n index. The A and B labels track the range of frequencies for which the $n = 0$ mode is evanescent, while the C label tracks the cutoff frequency of the $n = -1$ mode.

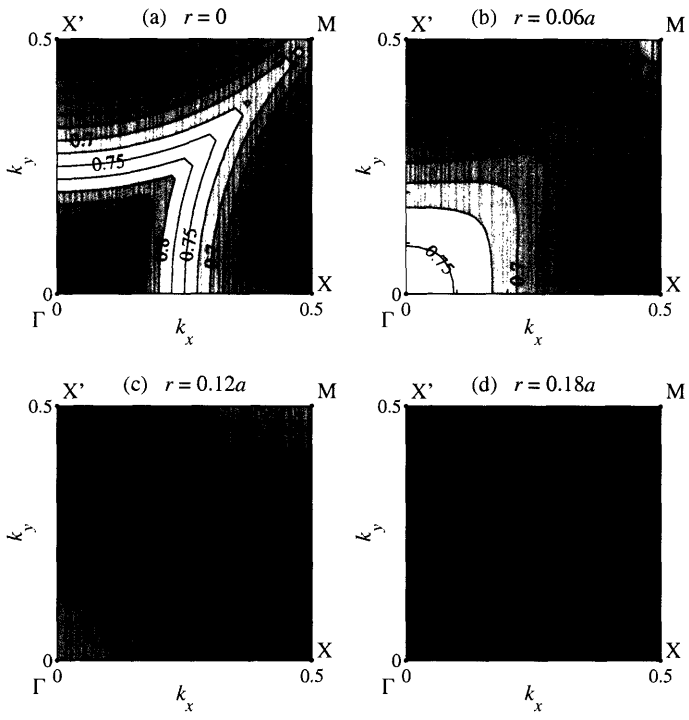

Figure 7-4: Contour plots of the second photonic crystal band $\omega(k_x, k_y)$ for varying radii of the dielectric rods: (a) $r = 0$ (vacuum), (b) $r = 0.06a$, (c) $r = 0.12a$, and (d) $r = 0.18a$. The same color scheme is used for all four parts of the figure. Constant-frequency contours are labelled by the corresponding value of the angular frequency ω in units of $(2\pi c/a)$. In parts (b), (c) and (d), a black dot indicates the position of the saddle point van Hove singularity.

the gap edge A. This ratio of almost 3 between the steepness of κ near the upper and lower band edges is also visible in Fig. 7-1(b) and is the main cause for the strong asymmetry of the localization strength along the waveguide mode dispersion relation (Fig. 7-1(c)).

7.4 General Arguments for the Existence of the Saddle Point

The presence of a saddle point in the second photonic band and the associated enhanced confinement is not just an accident for the particular parameters of the bulk

photonic crystal considered above. In Fig. 7-4(a–d) we present color contour plots of the dispersion relation of the second band for photonic crystals in which the radius r of the dielectric rods is increased from 0 to $0.06a$, $0.12a$, and $0.18a$. First, we see that for values of $r > 0$ the photonic band always has a saddle point van Hove singularity (shown as a black dot in Fig. 7-4(b–d)) in the middle of the band, away from the symmetry points. We argue that this saddle point must exist for $r > 0$ because (i) all points along the ΓM symmetry line are maxima in the direction perpendicular to ΓM and (ii) $\omega(k, k)$ has a minimum somewhere between Γ and M. Part (i) is due to a mirror symmetry across ΓM and to an anti-crossing between the second and third bands. Part (ii) comes from the combination of a normal tendency of the band to increase from M to Γ (as seen from the vacuum band in Fig. 7-4(a)) and a repulsion between bands 2 and 4. This repulsion is canceled at the M point because the two bands belong to different irreducible representations, but it becomes strong as we move away from the M point, and thus leads to the minimum in $\omega(k, k)$ [39]. From the same topological and perturbative arguments it follows that such an interior saddle point will be present in the TM and TE band structures of other square 2D photonic crystals as well. In principle, such saddle points can also be used to enhance band-gap confinement for other geometries, such as 2D photonic crystal slabs or 3D photonic crystals.

7.5 Summary

We have shown that a saddle-point van Hove singularity in a band adjacent to a photonic crystal band gap can lead to photonic crystal structures that defy the conventional wisdom according to which the strongest band-gap confinement is found at frequencies near the midgap. As an example of how this effect can be used to enhance band-gap confinement, we presented a two-dimensional square photonic crystal

waveguide. In general, the saddle point favors the appearance of a very flat photonic band which in turn results in an enhanced confinement at band-gap frequencies immediately above or below the flat band. This explains the recently observed anomalous radiation loss of a photonic crystal waveguide mode and suggests that, in general, one can make use of such saddle points to improve the design of other photonic devices that require band gap confinement.

Bibliography

[1] E. Yablonovitch. Inhibited spontaneous emission in solid-state physics and electronics. *Phys. Rev. Lett.*, 58:2059–2062, 1987.

[2] S. John. Strong localization of photons in certain disordered dielectric superlattices. *Phys. Rev. Lett.*, 58:2486–2489, 1987.

[3] J. D. Joannopoulos, R. D. Meade, and J. N. Winn. *Photonic Crystals: Molding the Flow of Light.* Princeton, 1995.

[4] J. D. Joannopoulos, P. R. Villeneuve, and S. Fan. Photonic crystals: putting a new twist on light. *Nature*, 386:143–149, 1997.

[5] K. Sakoda. *Optical Properties of Photonic Crystals.* Springer, 2001.

[6] S. G. Johnson and J. D. Joannopoulos. Three-dimensionally periodic dielectric layered structure with omnidirectional photonic band gap. *Appl. Phys. Lett.*, 77:3490–3492, 2000.

[7] M. H. Qi, E. Lidorikis, P. T. Rakich, S. G. Johnson, J. D. Joannopoulos, E. P. Ippen, and H. I. Smith. A three-dimensional optical photonic crystal with designed point defects. *Nature*, 429:538–542, 2004.

[8] M. Ibanescu, S. G. Johnson, M. Soljacic, J. D. Joannopoulos, Y. Fink, O. Weisberg, T. D. Engeness, S. A. Jacobs, and M. Skorobogatiy. Analysis of mode structure in hollow dielectric waveguide fibers. *Phys. Rev. E*, 67:046608, 2003.

[9] W. D. Warters. WT4 millimeter waveguide system: introduction. *Bell Syst. Tech. J.*, 56:1825–1827, 1977. The introduction to a special issue with many useful articles.

[10] M. Miyagi and S. Kawakami. Design theory of dielectric-coated circular metallic waveguides for infrared transmission. *J. Lightwave Tech.*, 2:116–126, 1984.

[11] Y. Matsuura and J. A. Harrington. Hollow glass waveguides with three-layer dielectric coating fabricated by chemical vapor deposition. *J. Opt. Soc. Am. A*, 14:1255–1259, 1997.

[12] S. G. Johnson, M. Ibanescu, M. Skorobogatiy, O. Weisberg, T. D. Engeness, M. Soljacic, S. A. Jacobs, J. D. Joannopoulos, and Y. Fink. Low-loss asymptotically single-mode propagation in large-core omniguide fibers. *Opt. Express*, 9:748–779, 2001.

[13] P. Yeh, A. Yariv, and E. Marom. Theory of Bragg fiber. *J. Opt. Soc. Am.*, 68:1196–1201, 1978.

[14] N. J. Doran and K. J. Bulow. Cylindrical Bragg fibers: a design and feasibility study for optical communications. *J. Lightwave Tech.*, 1:588–590, 1983.

[15] A. N. Lazarchik. Bragg fiber lightguides. *Radiotekhnika i electronika*, 1:36–43, 1988.

[16] C. M. de Sterke and I. M. Bassett. Differential losses in Bragg fibers. *J. Appl. Phys.*, 76:680–688, 1994.

[17] F. Brechet, P. Roy, J. Marcou, and D. Pagnoux. Singlemode propagation into depressed-core-index photonic-bandgap fibre designed for zero-dispersion propagation at short wavelengths. *Elec. Lett.*, 36(6):514–515, 2000.

[18] Y. Fink, J. N. Winn, S. Fan, C. Chen, J. Michel, J. D. Joannopoulos, and E. L. Thomas. A dielectric omnidirectional reflector. *Science*, 282:1679–1682, 1998.

[19] J. N. Winn, Y. Fink, S. Fan, and J. D. Joannopoulos. Omnidirectional reflection from a one-dimensional photonic crystal. *Optics Lett.*, 23:1573–1575, 1998.

[20] D. N Chigrin, A. V. Lavrinenko, D. A. Yarotsky, and S. V. Gaponenko. Observation of total omnidirectional reflection from a one-dimensional dielectric lattice. *Appl. Phys. A*, 68:25–28, 1999.

[21] Y. Fink, D. J. Ripin, S. Fan, C. Chen, J. D. Joannopoulos, and E. L. Thomas. Guiding optical light in air using an all-dielectric structure. *J. Lightwave Tech.*, 17:2039–2041, 1999.

[22] Y. Xu, R. K. Lee, and A. Yariv. Asymptotic analysis of Bragg fibers. *Optics Lett.*, 25:1756–1758, 2000.

[23] Y. Xu and A. Yariv. Asymptotic analysis of Bragg fibers and dielectric coaxial fibers. In Achyut Dutta, Abdul Ahad S. Awwal, Niloy K. Dutta, and Katsunari Okamoto, editors, *Proc. SPIE*, volume 4532, pages 191–205, 2001.

[24] T. Kawanishi and M. Izutsu. Coaxial periodic optical waveguide. *Optics Express*, 7(1):10–22, 2000.

[25] M. Ibanescu, Y. Fink, S. Fan, E. L. Thomas, and J. D. Joannopoulos. An all-dielectric coaxial waveguide. *Science*, 289:415–419, 2000.

[26] A. Argyros. Guided modes and loss in bragg fibers. *Optics Express*, 10(24):1411–1417, 2002.

[27] J. D. Jackson. *Classical Electrodynamics*. Wiley, New York, third edition, 1998.

[28] B. Temelkuran, S. D. Hart, G. Benoit, J. D. Joannopoulos, and Y. Fink. Wavelength-scalable hollow optical fibres with large photonic bandgaps for CO2 laser transmission. *Nature*, 420:650–653, 2002.

[29] R. A. Waldron. *Theory of Guided Electromagnetic Waves.* Van Nostrand Reinhold, London, 1969.

[30] B. E. A. Saleh and M. C. Teich. *Fundamentals of Photonics.* Wiley, New York 1991.

[31] S. E. Miller and A. G. Chynoweth, editors. *Optical Fiber Telecommunications.* Academic Press, New York, 1979.

[32] J. C. Knight, J. Broeng, T. A. Birks, and P. St.-J. Russell. Photonic band gap guidance in optical fibers. *Science*, 282:1476–1478, 1998.

[33] R. F. Cregan, B. J. Mangan, J. C. Knight, T. A. Birks, P. St.-J. Russell, and P. J. Roberts. Single-mode photonic band gap guidance of light in air. *Science*, 285:1537–1539, 1999.

[34] M. Miyagi, A. Hongo, Y. Aizawa, and S. Kawakami. Fabrication for germanium-coated nickel hollow waveguides for infrared transmission. *Appl. Phys. Lett.*, 43:430–432, 1983.

[35] A. Yariv. *Optical Electronics in Modern Communications.* Oxford Univ. Press, New York, 1997.

[36] Steven G. Johnson and J. D. Joannopoulos. Block-iterative frequency-domain methods for Maxwell's equations in a planewave basis. *Opt. Express*, 8(3):173–190, 2001.

[37] N. J. Cronin. *Microwave and Optical Waveguides.* Institute of Physics, Bristol, 1995.

[38] Y. Xu, R. K. Lee, and A. Yariv. Asymptotic analysis of dielectric coaxial fibers. *Optics Letters*, 27:1019–1021, 2002.

[39] M. Ibanescu, S. G. Johnson, D. Roundy, C. Luo, Y. Fink, and J. D. Joannopoulos. Anomalous dispersion relations by symmetry breaking in axially uniform waveguides. *Phys. Rev. Lett.*, 92:063903, 2004.

[40] P. St.-J. Russell. Photonic crystal fibers. *Science*, 299:358–362, 2003.

[41] J. E. Sipe. Vector k.p approach for photonic band structures. *Phys. Rev. E*, 62(4):5672–5677, 2000.

[42] P. J. B. Clarricoats and R. A. Waldron. Non-periodic slow-wave and backward-wave structures. *J. Electron. Contr.*, 8:455–458, 1960.

[43] P. J. B. Clarricoats. Circular-waveguide backward-wave structures. *Proc. IEEE*, 110:261–270, 1963.

[44] A. S. Omar and K. F. Schunemann. Complex and backward-wave modes in inhomogeneously and anisotropically filled waveguides. *IEEE Trans. Microwave Theory Tech.*, MTT-35(3):268–275, 1987.

[45] M. Mrozowski and J. Mazur. Predicting complex waves in lossless guides. In *Proc. 20th European Microwave Conf.*, volume 1, pages 487–492, Budapest, 1990.

[46] M. Mrozowski and J. Mazur. Matrix theory approach to complex waves. *IEEE Trans. Microwave Theory Tech.*, 40:781–785, 1992.

[47] A. Ashkin and J. M. Dziedzic. Radiation pressure on a free liquid surface. *Phys. Rev. Lett.*, 30:139–142, 1973.

[48] J. P. Gordon. Radiation forces and momenta in dielectric media. *Phys. Rev. A*, 8:14–21, 1973.

[49] D. F. Nelson. Momentum, pseudomomentum, and wave momentum: Toward resolving the minkowski-abraham controversy. *Phys. Rev. A*, 44:3985–3996, 1991.

[50] S. J. Smith and E. M. Purcell. Visible light from localized surface charges moving across a grating. *Phys. Rev.*, 92:1069, 1953.

[51] C. Luo, M. Ibanescu, S.G. Johnson, and J.D. Joannopoulos. Cherenkov radiation in photonic crystals. *Science*, 299:368–371, 2003.

[52] V.G. Veselago. The electrodynamics of substances with simultaneously negative values of epsilon and mu. *Sov. Phys. Usp.*, 10:509–514, 1968.

[53] L. Van Hove. The occurrence of singularities in the elastic frequency distribution of a crystal. *Phys. Rev.*, 89:1189–1193, 1953.

[54] N. Vats and S. John. Non-markovian quantum fluctuations and superradiance near a photonic band edge. *Phys. Rev. A*, 58:4168–4185, 1998.

[55] R. A. Fisher, editor. *Optical Phase Conjugation.* Academic Press, New York, 1983.

[56] M. F. Yanik and S. Fan. Stopping light all optically. *Phys. Rev. Lett.*, 92:083901, 2004.

[57] M. F. Yanik and S. Fan. Time reversal of light with linear optics and modulators. *Phys. Rev. Lett.*, 93:173903, 2004.

[58] M. Ibanescu, S. G. Johnson, D. Roundy, Y. Fink, and J. D. Joannopoulos. Microcavity confinement based on an anomalous zero group-velocity waveguide mode. *Opt. Lett.*, 30:552–554, 2005.

[59] K. J. Vahala. Optical microcavities. *Nature*, 424:839–846, 2003.

[60] O. Painter, R. K. Lee, A. Scherer, A. Yariv, J. D. O'Brien, P. D. Dapkus, and I. Kim. Two-dimensional photonic band-gap defect mode laser. *Science*, 284:1819–1821, 1999.

[61] M. Soljacic, M. Ibanescu, S. G. Johnson, J. D. Joannopoulos, and Y. Fink. Optical bistability in axially modulated omniguide fibers. *Optics Letters*, 28:516–518, 2003.

[62] J. Vuckovic and Y. Yamamoto. Photonic crystal microcavities for cavity quantum electrodynamics with a single quantum dot. *Appl. Phys. Lett.*, 82:2374–2376, 2003.

[63] D. Ochoa, R. Houdre, M. Ilegems, H. Benisty, T. F. Krauss, and C. J. M. Smith. Diffraction of cylindrical bragg reflectors surrounding an in-plane semiconductor microcavity. *Phys. Rev. B*, 61:4806–4812, 2000.

[64] J. Vuckovic, M. Loncar, H. Mabuchi, and A. Scherer. Design of photonic crystal microcavities for cavity qed. *Phys. Rev. E*, 65:016608, 2000.

[65] M. R. Watts, S. G. Johnson, H. A. Haus, and J. D. Joannopoulos. Electromagnetic cavity with arbitrary Q and small modal volume without a complete photonic bandgap. *Optics Letters*, 27:1785–1787, 2002.

[66] K. Srinivasan and O. Painter. Momentum space design of high-q photonic crystal optical cavities. *Optics Express*, 10:670–684, 2002.

[67] Y. Akahane, T. Asano, Song B. S., and S. Noda. High-Q photonic nanocavity in a two-dimensional photonic crystal. *Nature*, 425:944–947, 2003.

[68] S. G. Johnson, S. Fan, A. Mekis, and J. D. Joannopoulos. Multipole-cancellation mechanism for high-q cavities in the absense of a complete photonic band gap. *Appl. Phys. Lett.*, 78:3388–3390, 2001.

[69] A. Taflove and S. C. Hagness. *Computational Electrodynamics: The Finite-Difference Time-Domain Method.* Artech House, Norwood, MA, second edition, 2000.

[70] V. A. Mandelshtam and H.S. Taylor. Harmonic inversion of time signals and its applications. *Journal of Chemical Physics*, 107:6756–6769, 1997.

[71] A. Chutinan and S. Noda. Waveguides and waveguide bends in two-dimensional photonic crystal slabs. *Phys. Rev. B*, 62:4488–4492, 2000.

[72] A. Mekis, J. C. Chen, I. Kurland, S. Fan, P. R. Villeneuve, and J. D. Joannopoulos. High transmission through sharp bends in photonic crystal waveguides. *Phys. Rev. Lett.*, 77:3787–3790, 1996.

[73] M. Bayindir, E. Ozbay, B. Temelkuran, M. M. Sigalas, C. M. Soukoulis, R. Biswas, and K. M. Ho. Guiding, bending, and splitting of electromagnetic waves in highly confined photonic crystal waveguides. *Phys. Rev. B*, 63:081107, 2001.

[74] Z. Y. Li and K. M. Ho. Anomalous propagation loss in photonic crystal waveguides. *Phys. Rev. Lett.*, 92:063904, 2004.

[75] J. Smajic, Ch. Hafner, K. Rauscher, and D. Erni. Computation of radiation leakage in photonic crystal waveguides. In The Electromagnetics Academy, editor, *Progress in Electromagnetics Research Symposium PIERS 2004*, volume 1, pages 21–24, Pisa, 2004.

[76] Y.-C. Hsue and T.-J. Yang. Contour of the attenuated length of an evanescent wave at constant frequency within a band gap of photonic crystal. *Solid State Comm.*, 129:475–478, 2004.

[77] P. Bienstman and R. Baets. Optical modelling of photonic crystals and vcsels using eigenmode expansion and perfectly matched layers. *Opt. Quant. Electron.*, 33:327–341, 2001.